Contents lists available at ScienceDirect

Solar Energy

A new push–pull dye for semi-transparent *p*-type dye-sensitized solar cells: Tuning conjugation by sexithiophene chain engineering

Vincenzo Scarano [a], Lorenzo Gontrani [b], Ana Yancy Segura Zarate [c], Simone Galliano [c,d], Raffaele Borrelli [d], Marilena Carbone [b], Danilo Dini [e], Daniele Mirante [a], Marta Feroci [a], Matteo Bonomo [c,e,*], Leonardo Mattiello [a,*]

[a] *Department of Basic and Applied Sciences for Engineering (SBAI), Sapienza University of Rome, via Castro Laurenziano 7, 00161 Rome, Italy*
[b] *Department of Chemical Science and Technology - University of Rome "Tor Vergata", Via della Ricerca Scientifica 1, 00133 Rome, Italy*
[c] *Department of Chemistry, NIS Interdepartmental Centre and INSTM, University of Turin, Via Gioacchino Quarello 15/a, 10135 Turin, Italy*
[d] *Department of Agricultural, Forest and Food Sciences, University of Turin, Largo Paolo Braccini 2, 10095 Grugliasco, TO, Italy*
[e] *Department of Chemistry, Sapienza University of Rome, Piazzale Aldo Moro 5, 00185 Rome, Italy*

ARTICLE INFO

ABSTRACT

We report on the synthesis of two new dyes to be employed as sensitizers in *p*-type dye-sensitized solar cells (DSCs). The design of the two new molecules under consideration has been inspired by the state-of-art dye **PMI-6 T-TPA**. In particular, a specific engineering of the thiophene-based central core is here considered to favour structural planarity between an oligothiophenic π-spacer (a sexithiophene), and the acceptor and donor units made by peryleneimide (PMI) and triphenylamine (TPA) moieties, respectively. This leads to a wide absorption in the NIR with stabilization of the HOMO energy level in the resulting dyes, as supported by TD-DFT simulations and spectroscopic characterization. When tested as sensitizers in NiO_x-based *p*-type DSCs, **A6D** (with an Acceptor-π-Donor structure) outperforms both its counterpart with a Donor-π-Donor structure (**D6D**) and P1, a benchmark dye in the field of *p*-DSCs. With **A6D** dye-sensitizer the resulting DSC device presents the quite remarkable value of stabilized efficiency as high as 0.15 % when I^-/I_3^- is employed as redox couple and nano-structured NiO_x photocathode is thick less than 2 μm and does not contain any blocking layer. Notwithstanding the panchromatic feature of the sensitizer, **A6D**-based devices show an average visible transmittance (AVT) of 8 %. Such a result paves the way toward the application of these types of multifunctional dyes in semi-transparent solar cells.

1. Introduction

The exploitation of solar energy represents one of the most important resources to meet the continuous energy demand and to address global warming issues, largely caused by the widespread use of fossil fuels and the subsequent huge CO_2 emissions during operation phase [1]. Moreover, the sun is an inexhaustible and clean resource [2], and, straightforwardly, a very promising response to the possible risk of exhaustion of fossil fuels [3]. In recent decades, interest in photovoltaic technologies has achieved a significant increase and it was against this background that the DSCs have found their space. DSCs have been very successful since 1991 as Grätzel cells, photoelectrochemical devices consisting of a dye capable of sensitizing a *n*-type semiconductor (TiO₂), allowing light radiation absorption and its conversion into electricity

[4]. These photovoltaic cells have shown several advantages over the classic technologies based on silicon, carving out more and more important spaces in electronics through their peculiar characteristics, such as the ease of construction, low cost, flexibility, transparency, and the ability to also exploit indoor ambient diffused light [5,6]. During the last 30 years, in terms of photo-conversion efficiency, *n*-type DSCs (*n*-DSCs) have achieved significant progress, reaching certified efficiency as high as 15.2 % in 2022 [7]. In 1999, the first studies using organic dyes to sensitize p-type semiconductors (*p*-DSC) were published [8]. In contrast to *n*-DSC, where the current is generated by the transfer of an electron from the photo-excited dye to the *n*-type semiconductor conduction band, in *p*-DSC there is a hole injection from the HOMO of the photo-excited dye to the valence band of the *p*-type semiconductor (non stoichiometric NiO_x represent the most successful *p*-type semiconductor)

---

* Corresponding authors.
    E-mail addresses: leonardo.mattiello@uniroma1.it (M. Bonomo), matteo.bonomo@unito.it (L. Mattiello).

[9,10]. In short, the *p*-DSC functioning can be summarized as follows: an incident photon is absorbed by the dye that promotes an electron in a higher energy level, generating a hole in the molecule HOMO. The hole is transferred to the semiconductor valence band, while the electron in the excited state reduces the redox mediator, bringing the dye back to its electronic ground state. The circuit is completed with the oxidation of the electrolyte by the counter-electrode, restoring the initial situation [11]. *p*-DSC can have a second use and be coupled to *n*-DSC to build tandem *t*- DSCs. This combination can achieve higher efficiency, taking advantage of the fact that one of the two photoelectrodes can absorb the light transmitted by the other [6,12]. However, at present, either taken individually or in tandem, *p*-DSCs have several issues: in fact, their photoconversion efficiency is significantly lower than *n*-DSCs, mainly because of the unwanted electronic recombination reactions that occur between the holes of NiO_x semiconductor with the reduced dye (geminate recombination) and with the reduced redox shuttle [13,14]. To limit these processes research has focused on *pursuing* the development of new redox mediators and innovative dye molecular architectures together with new formulations of NiO-based electrodes [15].Over the past 30 years, several classes of compounds have been tested as *p*-DSC sensitizers and studies have identified the structural characteristics that a dye must have in order to improve its performance. Porphyrins are one of the most studied classes, which have very important characteristics in terms of thermal and photochemical stability [16]. Studies of molecule **PPorph** have been pioneering, because they have reported the hole injection mechanism that occurs between the HOMO orbital of the excited dye and the valence band of the semiconductor. **PPorph** reported a very low photoconversion efficiency for the rapid geminate recombination process [17]. In successive studies, the addition of electron acceptor and conjugated spacers has improved the efficiency of these zinc-porphyrin derivatives, reaching an efficiency of 0.056 % with the molecule **ZnP-CO₂H-eNDI** presenting naphthalene diimide as the electron withdrawing group and vinyl as spacer, using I-based redox mediators [18]. When perylenemonoimide (PMI) is selected as acceptor and di(p-carboxyphenyl)amine as donor group separated by a fluorene and zinc porphyrin, the resulting molecule **ZnP1** produced photoconversion devices with a photoconversion efficiency (PCE) of 0.92 using tris(acetylacetonate) iron complex-based system as redox couple. The latter system is characterized by displaying a lower redox potential with consequent generation of higher V_{OC} [19]. Fully organic sensitizers could be a valuable choice to improve the overall efficiency of *p*-DSCs [20]: 4,4-difluoro-4-bora-3a,4a-diaza-s-indacene derivatives (Bodipy) and metal-free phthalocyanines have been highly successful for their efficient photon harvesting and high molar extinction coefficient, photostability and fluorescence quantum yields [21–23]. Dye **7** (Bodipy derivative) and molecule **ZnPc2** (phthalocyanine) obtained PCE values of 0.20 % (redox couple: I_3^-/I^-) [24] and 0.191 % (redox couple: Co^{III}/Co^{II}) [25], respectively, thanks to the complex dynamics of excited state formation in phthalocyanines [26]. The diketopyrrolopyrrole family has been thoroughly investigated as well. The studies by Hammarström and co-workers have determined the effects of the structural changes on the performance of the dyes. The presence of a strong acceptor group and a thienyl carboxylic acid anchoring group have allowed these dyes to achieve high performance as in the case of **Th-DPP-NDI** that displayed an overall efficiency value of 0.44 % using I_3^-/I^- as redox couple [12,27–29]. Squaraines constitute another class of dye-sensitizers that are very interesting for the light-absorbing properties in the near IR. This has led researchers to investigate thoroughly their properties as *p*-DSCs dyes. The **p-SQ2** dye with a squaraine moiety as acceptor and TPA as donor with two anchoring carboxyl functions, obtained a PCE of 0.113 % using I_3^-/I^- as redox mediator [30]. The molecule **SQ-PMI-NDI**, on the other hand, obtained a η = 0.083 % (redox mediator: I_3^-/I^-), directly binding the squaraine moiety to the semiconductor through a carboxyl function and adding a second light-harvester (PMI) linked to the electron attractor naphthalenediimide (NDI) [31]. Some of us have synthesized a series of symmetrical squaraines that differ for the extent of

the electron conjugation and the electronic character of the electron substituents on the squaric ring as well as for the dyes simmetry [32]. The dye **VG11-C8**, which has a dicyano-vinyl electron withdrawing group conjugated with the squaric ring, has reported the best efficiency performance (η = 0.043 %) using I_3^-/I^- as redox shuttle [33,34]. More recently, Carella's group develops new class of panchromatic pyran-based dyes, specifically designed as *p*-type sensitizers. These molecules are composed of a central pyran core symmetrically conjugated with two donor groups (phenothiazine or carbazole units) and functionalized with different electron acceptor groups. **CB7** dye has achieved an excellent PCE of 0.076 % (electrolyte: HSE from Dyesol®), making it a promising candidate for use in *t*-DSCs [35,36].

From the rationalization of the results obtained by the different classes of *p*-type sensitizers [20], it has been observed that the molecular structures presenting a donor moiety separated from an acceptor group through a conjugated π-bridge, are particularly efficient as sensitizers in *p*-DSCs [37]. This arrangement would ensure a different localization of frontier molecular orbitals. Indeed, in these A-π-D structures, HOMO is localized close to the cathode surface with involvement of a strong electron coupling between the dye and the electrode. This maximizes charge injection (or hole extraction) efficiency [38]. LUMO is usually localized on the acceptor unit and it is closer to the electrolyte solution. Being localized far away from the NiO_x surface the geometry of LUMO promotes dye regeneration and avoids unwanted recombination reactions [39]. Push-pull dyes have shown their potential since 2008 when Qin *et al.* synthesized **P1** dye [40]. This has a donor TPA moiety with a carboxyl group that allows the anchoring of the molecule on the semiconductor surface and a dicyano-vinyl electron withdrawing group, separated by a thiophene ring [40]. Since then, **P1** has been commonly used as a benchmark reference for its fast, cost efficient and easy synthesis coupled with good photoconversion efficiency (0.166 % with I_3^-/I^- as redox mediator) [41]. Starting from the structure of **P1**, researchers spent a lot of efforts in varying the electron attractor unit [42]. The modification of the number of thiophene ring in the π spacer [43] or of the electron withdrawing core [44] led to ameliorated performances in the interval 0.20–0.32 % with I_3^-/I^- as redox mediator).

The real breakthrough in **P1**-derived dyes dates back to 2015, when Spiccia and co-workers proposed a new push–pull dye with a structure specifically designed for *p*-DSCs application, which led to a dramatic reduction of the unwanted recombination reactions: **PMI-6T-TPA**. This colorant is characterized by having a TPA electron donating group with two carboxyl anchor groups bound to a PMI moiety as electron acceptor, through a sexithiophene chain acting as a bridging π-spacer [45]. **PMI-6T-TPA**-sensitized electrodes showed a record PCE as high as 0.41 % in conjunction with I-based electrolytes. Such a remarkable value of PCE was further increased to 1.3 % and 2.51 % using cobalt tris(ethylene-amine) complex-based and a tris(acetylacetonate) iron complex-based systems as redox couples, respectively. Despite the observation of lower PCEs when I_3^-/I^- is employed as redox couple, the I-based redox system is the only one that can be employed in tandem devices [46]. In the footsteps of **PMI-6T-TPA**, several push–pull dyes have been proposed with modification on the anchoring unit [47] or the chemical nature of the conjugated spacer [48].

In this paper, taking as model **PMI-6T-TPA**, we synthesized a new organic dye (named **A6D**, Fig. 1). The structural modifications proposed in **A6D** with respect to **PMI-6T-TPA** involve the position and length of the alkyl chains in the oligothiophene bridging core. The aim is to increase the planarity of the molecule with beneficial effect on the electron conjugation and the extent of the electronic delocalization. This resulted in a wide absorption range for the new dye **A6D** and a PCE for the corresponding *p*-type device as high as 0.15 % (with I_3^-/I^- as mediator) when ultrathin (<2 μm) highly transparent NiO_x photocathodes were employed.
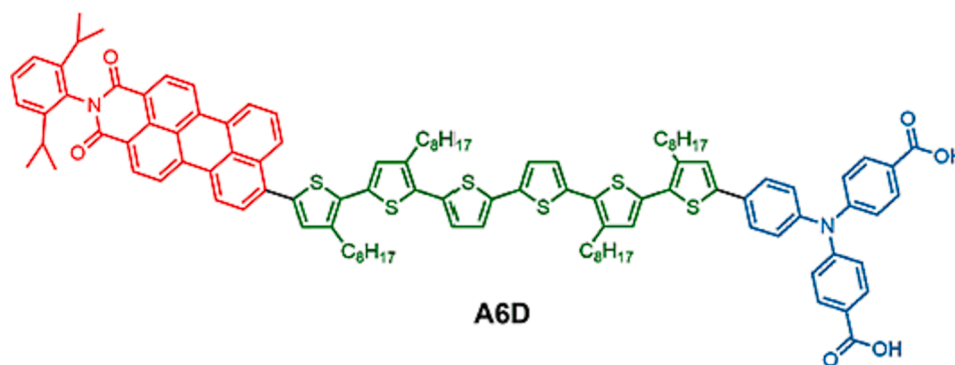
Fig. 1. Structure of the multifunctional dye-sensitizer **A6D**. The three main structural blocks of **A6D** are the (i) acceptor unit (PMI), (ii) bridging π-spacer and (iii) TPA donor unit which are coloured in red, green and blue, respectively. Electron injection occurs at TPA from the cathode (not shown) with the successive transfer of the injected charge from TPA to PMI through the sexithiophene spacer. PMI of **A6D** represents the site at which I_3 reduction takes place.

2. Experimental

Unless otherwise stated, all solvents and starting materials were analytically pure and used as received from commercial sources (Sigma–Aldrich, Fluorochem, TCI, Thermo Scientific and AlfaAesar) without further purification: *Perylene-3,4,9,10-tetracarboxylic dianhydride*, 97 % (CAS: 128–69-8) – Sigma-Aldrich, *Imidazole*, > 98 % (CAS: 288–32-4) – TCI, *2,6-Diisopropylaniline*, > 90 % (CAS: 24544–04-5) – TCI, *Zinc acetate dihydrate*, 98 % (CAS: 5970–45-6) – Fluorochem, *Bromine*, ≥ 99 % (CAS: 7726–95-6) – Sigma-Aldrich, *Bis(pinacolato)diboron*, 99 % (CAS: 73183–34-3) – Fluorochem, *1,1′-Bis(diphenylphosphino)ferrocenepalladium(II) dichloride* (*Pd(dppf)Cl₂*), 98 % (CAS: 72287–26-4) – Fluorochem, *Potassium acetate*, ≥ 99 % (CAS: 127–08-2) – Sigma-Aldrich, *2-Bromo-3-octylthiophene*, 97 % (CAS: 145543–83-5) – TCI, *2,2′-Bithiophene*, 99 % (CAS: 492–97-7) – Sigma-Aldrich, *Magnesium, turnings*, ≥ 99 % (CAS: 7439–95-5) – AlfaAesar, *1,2-Dibromoethane*, ≥ 98 % (CAS: 106–93-4) – Sigma-Aldrich, *tert-Butyl 4-Bromobenzoate*, 97 % (CAS: 59247–47-1) – Fluorochem, *Aniline*, ≥99 % (CAS: 62–53-3) – Sigma-Aldrich, *Tris(dibenzylideneacetone)dipalladium(0)* (*Pd₂(dba)₃*), 97 % (CAS: 51364–51-3) – Thermo Scientific Chemicals, *Tri-tert-butylphosphonium Tetrafluoroborate*, > 98 % (CAS: 131274–22-1) – TCI, *Potassium tert-butoxide*, ≥ 98 % (CAS: 865–47-4) – Sigma-Aldrich, *Potassium phosphate*, 97 % (CAS: 7778–53-2) – Thermo Scientific Chemicals, *Trifluoroacetic acid*, 99 % (CAS: 76–05-1) – Sigma-Aldrich. *Diethyl ether* was distilled by standard procedure [49] and readily used in syntheses. The reactions were carried out under an inert nitrogen atmosphere. The catalyst *dichloro[1,3-bis(diphenylphosphino)propane] nickel(II)* (*Ni(dppp) Cl₂*) used in the Kumada coupling reactions was synthesized using published procedures [50]. *N-Bromosuccinimide* (NBS) used in the bromination reactions was purified as reported in literature [51]. The product purification was performed by flash chromatography using Silica Gel 60 (0.04–0.063 mm). ^{1}H NMR and ^{13}C NMR spectra were obtained on a Bruker AVANCE 400 MHz spectrometer at 400 and 100 MHz, respectively. The residual signals for the NMR solvent (CDCl₃) are 77.16 ppm (^{13}C) and 7.26 ppm (^{1}H). Mass Spectroscopy were recorded by a Varian 320 MS TQ equipped with an electrospray ionization (ESI) operating either in positive or negative mode. The chemical structures of all the intermediates are reported in Appendix B, along with their NMR spectra. Absorbance was measured with a UV–vis spectrophotometer (Varian Cary 300 Bio, Agilent technologies) in a double beam geometry. To record UV–vis absorption spectra, each dye was dissolved in proper organic solvent with the latter used also as a reference. Cuvettes were made of quartz.

2.1. N-(2,6-diisopropylphenyl)perylene-3,4-dicarboximide (2)

A mixture of perylene-3,4,9,10-tetracarboxilic dianhydride **1** (232 mg, 0.60 mmol), imidazole (700 mg, 10.3 mmol), zinc acetate dihydrate (90 mg, 0.47 mmol), water (250 μL, 13.8 mmol) and 2,6-diisopropylaniline (86 mg, 0.48 mmol) was heated in autoclave at 180 °C for 24 h. After the reaction was completed, the mixture was first washed with concentrated HCl and centrifuged and then washed with water and centrifuged again. After removal of the supernatant, the precipitate was transferred with acetone into a flask, dried under reduced pressure and purified by flash column chromatography using chloroform as eluting medium to give **2**, as a red solid (152 mg, 53 % yield). ^{1}**H NMR** (400 MHz, CDCl₃): δ = 8.62 (d, *J* = 8.0 Hz, 2H), 8.42–8.38 (m, 4H), 7.86 (d, *J* = 8.0 Hz, 2H), 7.61 (t, *J* = 7.8 Hz, 2H), 7.51–7.44 (m, 1H), 7.35 (d, *J* = 7.8 Hz, 2H), 2.78 (sep, *J* = 6.8 Hz, 2H), 1.20 (d, *J* = 6.9 Hz, 12H); ^{13}**C NMR** (100 MHz, CDCl₃): δ = 164.14, 145.84, 137.64, 134.42, 132.13, 131.20, 131.08, 130.68, 129.58, 129.32, 128.09, 127.19, 127.15, 124.16, 123.96, 121.12, 120.31, 29.30, 24.17.

2.2. 9-bromo-N-(2,6-diisopropylphenyl)perylene-3,4-dicarboximide (3)

610 mg (1.27 mmol) of **2** were dissolved in 60 mL of dichloromethane and 610 mg (196 μL, 3.81 mmol) of Br₂ were added dropwise. The solution was stirred and refluxed for 5 h. The reaction mixture was cooled and washed three times with 60 mL of a saturated solution of sodium thiosulphate (Na₂S₂O₃) to remove the excess bromine and washed with 60 mL of water once. The organic phase was collected and dried over anhydrous Na₂SO₄. After filtration, the solvent was removed at reduced pressure. The crude product was purified by flash column chromatography using chloroform as eluent and the pure product **3** was isolated as a red solid (581 mg, yield 82 %). ^{1}**H NMR** (400 MHz, CDCl₃): δ = 8.68–8.64 (m, 2H), 8.50 (d, *J* = 7.6 Hz, 1H), 8.47 (d, *J* = 8.1 Hz, 1H), 8.42 (d, *J* = 8.1 Hz,1H), 8.31 (d, *J* = 8.4 Hz, 1H), 8.25 (d, *J* = 8.2 Hz, 1H), 7.92 (d, *J* = 8.2 Hz, 1H), 7.73 (t, *J* = 8.0 Hz, 1H), 7.48 (t, *J* = 7.8 Hz, 1H), 7.34 (d, *J* = 7.8 Hz, 2H), 2.77 (sep, *J* = 6.8 Hz, 2H), 1.18 (d, *J* = 6.9 Hz, 12H).

2.3. N-(2,6-diisopropylphenyl)-9-(4,4,5,5-tetramethyl-[1–3] dioxaborolan-2-yl)perylen-3,4-dicarboximide (A)

580 mg (1.03 mmol) of **3**, 508 mg (2.0 mmol) of bis(pinacolato) diboron, 245 mg (2.5 mmol) of potassium acetate (KOAc) and 37 mg (0.05 mmol) of catalyst Pd(dppf)Cl₂ were added in 15 mL of dioxane. The resulting suspension was stirred and degassed overnight at 90 °C. After cooling at room temperature, the solvent was removed under reduced pressure. The crude product was purified by flash column chromatography (dichloromethane as eluting medium) and the final product **A** was isolated as a red solid (276 mg, 44 % yield). ^{1}**H NMR** (400 MHz, CDCl₃): δ = 8.81 (d, *J* = 8.4 Hz, 1H) 8.63–8.58 (m, 2H), 8.38–8.31 (m, 4H), 8.16 (d, *J* = 7.5 Hz, 1H), 7.59 (t, *J* = 8.1 Hz, 1H), 7.49 (t, *J* = 7.8 Hz, 1H), 7.37 (d, *J* = 7.8 Hz, 2H), 2.79 (sep, *J* = 6.8 Hz, 2H), 1.48 (s, 12H), 1.20 (d, *J* = 6.9 Hz, 12H); ^{13}**C NMR** (100 MHz,

CDCl$_3$): δ = 164.15, 164.09, 145.86, 138.03, 137.93, 137.32, 136.28, 132.13, 131.92, 131.80, 131.67, 131.25, 130.48, 129.56, 128.96, 127.59, 127.21, 126.90, 124.14, 123.69, 122.80, 121.39, 120.82, 120.28, 84.40, 29.30, 25.15, 24.16.

2.4. 5,5′-dibromo-2,2′-bithiophene (5)

In a flask containing 1.02 g (6.1 mmol) of 2,2′-bithiophene (**4**) solubilised in 30 mL of a 1:1(v/v) mixture of chloroform - acetic acid, 2.28 g (12.8 mmol) of N-bromosuccinimide (NBS) were added in small portions at 0 °C, under stirring and nitrogen flow. The reaction is maintained at room temperature for 2 h. The reaction was quenched by addition of water and the mixture was extracted with CH$_2$Cl$_2$. The organic layers were washed with a saturated solution of sodium bicarbonate (NaHCO$_3$), brine and dried with anhydrous sodium sulphate (Na$_2$SO$_4$). After filtration and solvents removal, the product **5** was obtained as a white/gray solid (1.96 g, 99 % yield). **^{1}H NMR** (200 MHz, CDCl$_3$): δ = 6.97 (d, J = 3.8 Hz, 2H), 6.85 (d, J = 3.8 Hz, 2H); **^{13}C NMR** (50 MHz, CDCl$_3$): δ = 137.91, 130.79, 124.27, 111.65.

2.5. 3-octyl-2-thienylmagnesium bromide (7)

Magnesium turnings (0.66 g, 27 mmol), previously grinded, were transferred in an oven-dry 100 mL round-bottomed flask. Freshly distilled diethyl ether is added (20 mL) under nitrogen flow. Subsequently, a solution of 2-bromo-3-octylthiophene (**6**, 3.71 g, 13.5 mmol) and 1,2-dibromoethane (580 μL, 1.27 g, 6.75 mmol) in distilled diethyl ether was added dropwise. The reaction was heated at reflux under nitrogen for 6 h. The resulting Grignard reagent (**7**) was used immediately in subsequent coupling reactions.

2.6. 3,3′′′-dioctyl-2,2′:5′,2′′:5′′,2′′′-quaterthiophene (8)

1.62 g (5 mmol) of compound **5** and 272 mg (0.5 mmol) of dichloro [1,3-bis(diphenylphosphino)propane] nickel (II) (Ni(dppp)Cl$_2$) were added to a 100 mL three-necked flask in 20 mL of freshly distilled diethyl ether (Et$_2$O), under nitrogen flow. The solution was cooled to 0 °C in an ice bath and then a Et$_2$O solution of **7**, previously synthesized from 2-bromo-3-octylthiophene (**6**, 3.71 g, 13.5 mmol), was added dropwise. Once the additions were complete, the solution was heated to reflux (40 °C) and stirred under an inert atmosphere for 2 h. Next, the mixture was quenched at 0 °C with hydrochloric acid solution (1 M) until the end of the effervescence and was extracted three times with diethyl ether. The combined organic layers were washed with water and brine, and then dried over Na$_2$SO$_4$. After filtration, the solvent was removed under reduced pressure and the crude product was purified by silica gel flash chromatography with petroleum ether as eluent to give the pure compound **8** as a yellow oil (2.1 g, 76 % yield). **^{1}H NMR** (400 MHz, CDCl$_3$): δ = 7,18 (d, J = 5.2 Hz, 2H), 7.13 (d, J = 3.8 Hz, 2H), 7.03 (d, J = 3.8 Hz, 2H), 6.95 (d, J = 5.2 Hz, 2H), 2.79 (t, J = 7.7 Hz, 4H), 1.70–1.63 (m, 4H), 1.29 (m, 20H), 0.89 (app. t, J = 7.2 Hz, 6H); **^{13}C NMR** (100 MHz, CDCl$_3$): δ = 140.02, 136.94, 135.45, 130.45, 130.22, 126.66, 123.99, 123.95, 32.03, 30.81, 29.68, 29.57, 29.41, 29.40, 22.83, 14.26.

2.7. 5,5′′′-dibromo-3,3′′′-dioctyl-2,2′:5′,2′′:5′′,2′′′-quaterthiophene (9)

In a flask containing 2.1 g (3.8 mmol) of **8** in 50 mL of a 1:1(v/v) mixture of chloroform - acetic acid, 1.41 g (7.9 mmol) of N-bromosuccinimide (NBS) were added in small portions at 0 °C, under stirring and nitrogen flow. The reaction is maintained at room temperature for 4 h. The reaction was quenched by addition of water and the mixture was extracted with CH$_2$Cl$_2$. The organic layers were washed with a saturated solution of NaHCO$_3$ (three times), water and brine and dried with anhydrous Na$_2$SO$_4$. After filtration and solvents removal, the product **9** was obtained as a green/yellow solid (2.70 g, quantitative). **^{1}H NMR** (400 MHz, CDCl$_3$): δ = 7.10 (d, J = 3.8 Hz, 2H), 6.96 (d, J = 3.7 Hz, 2H),

6.90 (s, 2H), 2.71 (t, J = 7.7 Hz, 4H), 1.65–1.58 (m, 4H), 1.28 (m, 20H), 0.88 (app. t, J = 7.2 Hz, 6H); **^{13}C NMR** (100 MHz, CDCl$_3$): δ = 140.65, 137.17, 134.20, 132.84, 131.84, 127.08, 124.12, 110.80, 32.02, 30.65, 29.55, 29.51, 29.37, 29.34, 22.82, 14.26.

2.8. 3,3′′′′,3′′′′′,4′-tetraoctyl-2,2′:5′,2′′:5′′,2′′′:5′′′,2′′′′:5′′′′,2′′′′′-sexithiophene (10)

2.70 g (3.8 mmol) of compound **9** and 0.21 g (0.38 mmol) of dichloro [1,3-bis(diphenylphosphino)propane] nickel (II) (Ni(dppp)Cl$_2$) were added to a 100 mL three-necked flask in 20 mL of freshly distilled diethyl ether (Et$_2$O), under nitrogen flow. The solution was cooled to 0 °C in an ice bath and then a Et$_2$O solution of **7**, previously synthesized from 2-bromo-3-octylthiophene (**6**, 2.96 g, 10.75 mmol), was added dropwise. Once the additions were complete, the solution was heated to reflux (40 °C) and stirred under an inert atmosphere for 3 h. Next, the mixture was quenched at 0 °C with hydrochloric acid solution (1 M) until the end of the effervescence and was extracted three times with diethyl ether. The combined organic layers were washed with water and brine, and then dried over Na$_2$SO$_4$. After filtration, the solvent was removed under reduced pressure and the crude product was purified by silica gel flash chromatography with petroleum ether as eluting medium to give the pure compound **10** as an orange oil (1.97 g, 55 % yield). **^{1}H NMR** (400 MHz, CDCl$_3$): δ = 7.17 (d, J = 5.2 Hz, 2H), 7.15 (d, J = 3.8 Hz, 2H), 7.06 (d, J = 3.8 Hz, 2H), 6.96 (s, 2H), 6.94 (d, J = 5.2 Hz, 2H), 2.80 (t, J = 7.8 Hz, 8H), 1.74–1.63 (m, 8H), 1.29 (m, 40H), 0.88 (app. t, J = 7.0 Hz, 12H); **^{13}C NMR** (100 MHz, CDCl$_3$): δ = 140.16, 139.86, 136.88, 135.19, 134.53, 130.57, 130.30, 130.26, 128.89, 126.47, 124.03, 123.81, 32.05, 30.83, 30.68, 29.70, 29.58, 29.43, 22.83, 14.27.

2.9. 5-bromo-3,3′′′′,3′′′′′,4′-tetraoctyl-2,2′:5′,2′′:5′′,2′′′:5′′′,2′′′′:5′′′′,2′′′′′-sexithiophene (B)

In a flask containing 1.70 g (1.8 mmol) of **10** solubilized in 60 mL of a 1:1(v/v) mixture of chloroform - acetic acid, 0.375 g (2.1 mmol) of N-bromosuccinimide (NBS) were added in small portions in a time space of 4 h at 0 °C, under stirring and nitrogen flow. After the addition, the reaction is maintained at room temperature for 4 h. The reaction was quenched by addition of water and the mixture was extracted with CH$_2$Cl$_2$. The organic layers were washed with a saturated solution of NaHCO$_3$ (three times), water and brine and dried with anhydrous Na$_2$SO$_4$. After filtration, the solvent was removed under reduced pressure and the crude product was purified by silica gel flash chromatography with petroleum ether as eluting medium to give the pure compound **B** as a dark orange oil (0.81 g, 44 % yield). **^{1}H NMR** (400 MHz, CDCl$_3$): δ = 7.17 (d, J = 5.1 Hz, 1H), 7.15–7.14 (m, 2H), 7.06–7.04 (m, 2H), 6.96 (s, 1H), 6.94 (d, J = 5.1 Hz, 1H), 6.90 (app. s, 2H), 2.82–2.71 (m, 8H), 1.72–1.59 (m, 8H), 1.30 (m, 40H), 0.89 (app. t, J = 7.0 Hz, 12H); **^{13}C NMR** (100 MHz, CDCl$_3$): δ = 140.37, 140.15, 139.83, 137.11, 136.75, 135.29, 134.57, 133.08, 132.85, 132.12, 130.87, 130.26, 130.23, 129.20, 128.86, 126.61, 126.43, 124.08, 124.00, 123.78, 110.51, 32.04, 30.82, 30.67, 30.64, 29.70, 29.69, 29.58, 29.53, 29.44, 29.40, 29.38, 22.83, 14.26.

2.10. 4-(N-Phenylamino)benzoic acid tert-butyl ester (12)

In a two-necked flask containing 20 mL of dry toluene, 0.86 g (3.34 mmol) of *tert*-butyl 4-bromobenzoate (**11**) and 0.47 g (520 μL, 5.05 mmol) of aniline were dissolved. The solution was stirred and degassed under nitrogen flow for 10 min. Next, 0.85 g (7.6 mmol) of potassium *tert*-butylate (t-BuOK), 154 mg (0.17 mmol) of Tris(dibenzylideneacetone)dipalladium(0) (Pd$_2$dba$_3$) and 78 mg (0.27 mmol) of tri-*tert*-butylphosphonium tetrafluoroborate ([HP(t-Bu)$_3$]BF$_4$) were added. The mixture was heated at 40 °C and stirred under an inert atmosphere for 3 h. The reaction was quenched with the addition of water and the aqueous phase was neutralized with a solution (1 M) of HCl (a slight

colour change is observed at the neutralization point) and the aqueous and organic phases were extracted with CH_2Cl_2 (three times). The organic phase is collected and dried with anhydrous Na_2SO_4, filtered and the solvent was removed under reduced pressure. A yellow–brown solid was obtained, which was purified by flash column chromatography using petroleum ether / CH_2Cl_2 [1:1] as eluting medium to give the pure compound **12**, which appears as a white solid (0.71 g, 79 % yield). **1H NMR** (400 MHz, $CDCl_3$): $\delta = 7.89$ (app. d, $J = 8.8$ Hz, 2H), 7.35–7.31 (m, 2H), 7.16 (app. d, $J = 8.8$ Hz, 2H), 7.05 (app. t, $J = 7.5$ Hz, 1H), 7.03–6.98 (m, 2H), 1.59 (s, 9H); **13C NMR** (100 MHz, $CDCl_3$): $\delta = $ 165.93, 147.80, 141.17, 131.18, 129.28, 122.55, 119.92, 114.55, 80.13, 28.19.

2.11. N,N-Di(4-benzoic acid tert-butyl ester)phenylamine (13)

In a two-necked flask containing 10 mL of dry toluene, 530 mg (2.06 mmol) of *tert*-butyl 4-bromobenzoate **11** and 510 mg (1,90 mmol) of diphenylamine **12** were dissolved. The solution was stirred and degassed under nitrogen flow for 10 min. Next, 444 mg (3.96 mmol) of potassium *tert*-butylate (t-BuOK), 87 mg (0.095 mmol) of Tris(dibenzylideneacetone)dipalladium(0) (Pd_2dba_3) and 44 mg (0.153 mmol) of tri-*tert*-butylphosphonium tetrafluoroborate ($[HP(t-Bu)_3]BF_4$) were added. The mixture was heated at 80 °C and stirred under an inert atmosphere for 3 h. The reaction was quenched with the addition of water and the aqueous phase was neutralized with a solution (1 M) of HCl (a slight color change is observed at the neutralization point) and the aqueous and organic phases were extracted with CH_2Cl_2 (three times). The organic phase is collected and dried with anhydrous Na_2SO_4, filtered and the solvent was removed under reduced pressure. The crude product was purified by flash column chromatography using CH_2Cl_2 / petroleum ether [2:1] as eluting medium to give the pure compound **13**, which appears as a white solid (660 mg, 78 % yield). **1H NMR** (400 MHz, $CDCl_3$): $\delta = 7.86$ (app. d, $J = 8.8$ Hz, 4H), 7.32 (app. t, $J = 8.4$ Hz, 2H), 7.18–7.16 (m, 1H), 7.13–7.11 (m, 2H), 7.06 (app. d, $J = 8.8$ Hz, 4H), 1.58 (s, 18H); **13C NMR** (100 MHz, $CDCl_3$): $\delta = 165.54$, 150.89, 146.44, 130.93, 129.88, 126.43, 126.20, 125.21, 122.55, 80.84, 28.38.

2.12. N,N-Di(4-benzoic acid tert-butyl ester)-4-bromo-phenylamine (14)

In a flask, 1.08 g (2.42 mmol) of triphenylamine **13** were dissolved in 6 mL of dry *N,N*-Dimethylformamide (DMF) and stirred in an ice bath. NBS (0.52 g, 2.93 mmol) was added in small portions at 0 °C and then, the mixture was left to react at RT overnight. The solvent was removed under reduced pressure and the obtained solid was crystallized with ethanol. The white crystals of pure product **14** (0.98 g, 77 % yield) were filtered off and dried in vacuum. **1H NMR** (400 MHz, $CDCl_3$): $\delta = 7.86$ (app. d, $J = 8.6$ Hz, 4H), 7.40 (app. d, $J = 8.6$ Hz, 2H), 7.04 (app. d, $J = 8,8$ Hz, 4H), 6.98 (app. d, $J = 8.8$ Hz, 2H), 1.57 (s, 18H); **13C NMR** (100 MHz, $CDCl_3$): $\delta = 163.51$, 148.97, 145.58, 132.91, 131.04, 127.49, 126.70, 123.61, 117.81, 80.95, 28.35.

2.13. N,N-Di(4-benzoic acid tert-butyl ester)-4-(4,4,5,5-tetramethyl-[1–3]dioxaborolan-2-yl)-phenylamine (C)

810 mg (1.54 mmol) of compound **14**, 978 mg (3.85 mmol) of bis (pinacolato)diboron, 422 mg (4.31 mmol) of potassium acetate (KOAc) and 112 mg (0.154 mmol) of [1,1′-Bis(diphenylphosphino)ferrocene] dichloropalladium(II) [$Pd(dppf)Cl_2$] were dissolved in 20 mL of dioxane, the brown suspension was heated at 80 °C and stirred under nitrogen flow overnight. After the reaction was completed, the crude product was filtered on a short silica column with CH_2Cl_2 as eluent to remove catalytic residues. After solvent removal, the addition of 100 mL of hot methanol allowed the product to crystallize. The white crystals of pure product **C** (645 mg, 73 % yield) were filtered off and dried in vacuum. **1H NMR** (400 MHz, $CDCl_3$): $\delta = 7.86$ (app. d, $J = 8,7$ Hz, 4H), 7.74 (app. d, $J = 8,2$ Hz, 2H), 7.10–7.06 (m, 6H), 1.58 (s, 18H), 1.34 (s,

12H); **13C NMR** (100 MHz, $CDCl_3$): $\delta = 165.48$, 150.63, 149.15, 136.37, 130.95, 126.68, 124.57, 123.22, 83.97, 80.92, 28.37, 25.00.

2.14. 5-([N-(2,6-Diisopropylphenyl)]-9-perylenyl-3,4-dicarboximide)-3,3′′′′,3′′′′′,4′-tetraoctyl-2,2′:5′,2′:5′′,2′′:5′′′,2′′′:5′′′′,2′′′′′-sexithiophene (15)

95 mg (0.156 mmol) of block **A** and 105 mg (0.103 mmol) of block **B** were dissolved in 6 mL of dimethoxyethane (DME) and the solution was carefully degassed. Then, 310 μL (0.620 mmol) of a 2 M tripotassium phosphate solution were added. After further degassing, 14 mg (0.0156 mmol) of $Pd_2(dba)_3$ and 9 mg (0.0313 mmol) of $[HP(t-Bu)_3]BF_4$ were added and the resulting suspension was stirred at room temperature for 24 h. After the reaction was completed, it was poured into water and it was extracted with dichloromethane. The organic phases were dried with sodium sulfate and, after the solvent removal, the crude product was purified by flash column chromatography (dichloromethane / petroleum ether [2:1] as eluent) and the final product **15** was isolated as a black solid (103 mg, 70 % yield). **1H NMR** (400 MHz, $CDCl_3$): $\delta = $ 8.63–8.59 (m, 2H), 8.47 (d, $J = 8.4$ Hz, 1H), 8.40–8.29 (m, 4H), 7.70 (d, $J = 8.0$ Hz, 1H), 7.64 (t, $J = 8.0$ Hz, 1H), 7.51 (t, $J = 7.8$ Hz, 1H), 7.38 (d, $J = 7.8$ Hz, 2H), 7.21 (s, 1H), 7.18–7.05 (m, 6H), 6.96 (s, 1H), 6.94 (d, $J = 5.2$ Hz, 1H), 2.92 (t, $J = 7.9$ Hz, 2H), 2.86–2.78 (m, 8H), 1.83–1.63 (m, 8H), 1.32 (m, 40H), 1.24 (d, $J = 6.8$ Hz, 12H), 0.92–0.89 (m, 12H); **13C NMR** (100 MHz, $CDCl_3$): $\delta = 164.05$, 164.03, 145.81, 140.50, 139.86, 137.51, 137.16, 135.29, 132.40, 132.02, 131.59, 131.21, 130.87, 130.49, 130.22, 130.18, 129.57, 129.40, 129.07, 128.92, 128.79, 128.55, 127.36, 126.80, 126.56, 126.39, 124.14, 124.12, 124.04, 123.83, 123.42, 121.02, 64 120.96, 120.37, 120.19, 32.04, 32.03, 30.86, 30.81, 30.69, 30.66, 29.81, 29.73, 29.69, 29.69, 29.60, 29.57, 29.56, 29.52, 29.48, 29.44, 29.43,29.42, 29.33, 24.18, 22.83, 22.82, 14.27, 14.26. **ESI-MS** calculated for $C_{90}H_{105}NO_2S_6$ $[M + H]^+$ 1425.65 (100 %) and 1424.65 (96.7 %), found: 1425.56 (100 %) and 1424.52 (95.8 %).

2.15. 5-([N-(2,6-Diisopropylphenyl)]-9-perylenyl-3,4-dicarboximide)-5′′′′′-bromo-3,3′′′′,3′′′′′,4′-tetraoctyl-2,2′:5′,2′:5′′,2′′:5′′′,2′′′:5′′′′,2′′′′′-sexithiophene (16)

In a flask containing 62 mg (0.044 mmol) of compound **15** solubilized in 15 mL of a 1:1(v/v) mixture of chloroform - acetic acid, 9.4 mg (0.053 mmol) of N-bromosuccinimide (NBS) were added in small portions at 0 °C, under stirring. The reaction is maintained at room temperature for 24 h. The reaction was quenched by addition of water and the mixture was extracted with CH_2Cl_2. The organic layers were washed three times with a saturated solution of $NaHCO_3$ and once with water and dried with anhydrous Na_2SO_4. After filtration and solvents removal, the product **16** was obtained as a black solid (66 mg, quantitative). **1H NMR** (400 MHz, $CDCl_3$): $\delta = 8.67$–8.64 (m, 2H), 8.50–8.42 (m, 5H), 7.74 (d, $J = 7.9$ Hz, 1H), 7.69 (t, $J = 8.0$ Hz, 1H), 7.49 (t, $J = 7.8$ Hz, 1H), 7.36 (d, $J = 7.8$ Hz, 2H), 7.20 (s, 1H), 7.17–7.15 (m, 2H), 7.10—7.05 (m, 3H), 6.89 (app. s, 2H), 2.91 (t, $J = 7.9$ Hz, 2H), 2.85–2.76 (m, 6H), 2.72 (t, $J = 7,9$ Hz, 2H), 1.82–1,58 (m, 8H), 1.30 (m, 40H), 1.20 (d, $J = 6.9$ Hz, 12H), 0.90–0.87 (m, 12H); **13C NMR** (100 MHz, $CDCl_3$): $\delta = 164.11$, 145.86, 140.51, 140.43, 140.39, 140.23, 137.71, 137.39, 137.01, 135.43, 135.08, 133.14, 132.89, 132.59, 132.35, 132.20, 132.06, 131.66, 131.20, 130.86, 130.66, 129.88, 129.59, 129.25, 129.21, 129.15, 129.11, 129.04,128.99, 128.71, 127.53, 127.00, 126.67, 126.63, 124.28, 124.16, 124.13, 123.56, 121.15, 121.10, 120.55, 120.38, 110.54, 32.06, 32.03, 30.85, 65 30.70, 30.68, 30.65, 29.80, 29.76, 29.73, 29.69, 29.61, 29.57, 29.52, 29.48, 29.45, 29.42, 29.39, 29.37, 29.30, 24.17, 22.85, 22.83, 14.27. **ESI-MS** calculated for $C_{90}H_{104}BrNO_2S_6$ $[M + H]^+$ 1504.56, found:1504.28.

2.16. Di-tert-butyl 4,4'-[(4-{5'''''-([N-(2,6-Diisopropylphenyl)]-9-perylenyl-3,4-dicarboximide)-3,3'''',3''''',4'-tetraoctyl-2,2':5',2'':5'',2''':5''',2'''':5'''',2'''''-sexithiophen-5-yl}phenyl)imino] dibenzoate (17)

24 mg (0.042 mmol) of block **C** and 48 mg (0.032 mmol) of **16** were dissolved in 5 mL of dimethoxyethane (DME) and the solution was carefully degassed. Then, 84 μL (0.168 mmol) of a 2 M tripotassium phosphate solution were added. After further degassing, 3.8 mg (0.0042 mmol) of $Pd_2(dba)_3$ and 2.4 mg (0.0084 mmol) of $[HP(t-Bu)_3]BF_4$ were added and the resulting suspension was stirred at room temperature for 24 h. After the reaction was completed, it was poured into water and it was extracted with dichloromethane. The organic phases were dried with sodium sulfate and, after the solvent removal, the crude product was purified by flash column chromatography using dichloromethane as eluting medium and the final product **17** was isolated as a black solid (46 mg, 75 % yield). **^{1}H NMR** (400 MHz, CDCl$_3$): δ = 8.64–8.61 (m, 2H), 8.48 (d, J = 8.5 Hz, 1H), 8.45–8.35 (m, 4H), 7.90 (app. d, J = 8.7 Hz, 4H), 7.72 (d, J = 7.8 Hz, 1H), 7.66 (t, J = 8.0 Hz, 1H), 7.55–7.48 (m, 3H), 7.36 (d, J = 7.8 Hz, 2H), 7.21 (s, 1H), 7.17–7.09 (m, 12H), 7.00 (s, 1H), 2.92 (t, J = 7.8 Hz, 2H), 2.85–2.77 (m, 8H), 1.83–1.67 (m, 8H), 1.61 (s, 18H), 1.31 (m, 40H), 1.22 (d, J = 6.8 Hz, 12H), 0.91–0.88 (m, 12H); **^{13}C NMR** (100 MHz, CDCl$_3$): δ = 165.46, 164.07, 164.05, 150.56, 145.82, 145.67, 140.48, 140.25, 137.59, 137.27, 137.05, 135.36, 132.48, 132.09, 131.64, 131.21, 131.01, 130.68, 130.57, 130.12, 129.57, 129.49, 129.12, 128.97, 128.88, 128.63, 127.44, 126.89, 126.80, 126.59, 126.58, 126.56, 126.54, 126.46, 126.23, 126.18, 124.20, 124.14, 124.12, 124.08, 123.48, 122.86, 121.09, 121.03, 120.45, 120.28, 80.91, 32.04, 30.84, 30.68, 30.65, 29.80, 29.76, 29.72, 29.60, 29.58, 29.48, 29.44, 29.43, 29.31, 28.37, 24.17, 22.84, 22.83, 14.27.

2.17. 4,4'-[(4-{5'''''-([N-(2,6-Diisopropylphenyl)]-9-perylenyl-3,4-dicarboximide)-3,3'''',3''''',4'-tetraoctyl-2,2':5',2'':5'',2''':5''',2'''':5'''',2'''''-sexithiophen-5-yl}phenyl)imino] dibenzoic acid (A6D)

45 mg (0.024 mmol) of **17** were dissolved in 1 mL of CH$_2$Cl$_2$. Next, 0.2 mL of trifluoroacetic acid were added. The resulting solution was stirred at room temperature for 6 h. After the solvent removal, the final product **A6D** was obtained quantitatively, as a black solid (42 mg, quantitative). **^{1}H NMR** (400 MHz, CDCl$_3$): δ = 8.70–8.68 (m, 2H), 8.54–8.47 (m, 5H), 8.01 (app. d, J = 8,6 Hz, 4H), 7.77 (d, J = 7.8 Hz, 1H), 7.72 (t, J = 7.9 Hz, 1H), 7.59 (app. d, J = 7.9, 2H), 7.49 (t, J = 7.8 Hz, 1H), 7.35 (d, J = 7.8 Hz, 2H), 7.21–7.01 (m, 14H), 2.91 (t, J = 7.3 Hz, 2H), 2.85–2.68 (m, 8H), 1.79–1.67 (m, 8H), 1.19 (d, J = 6.8 Hz, 12H), 0.90–0.87 (m, 12H). **^{13}C NMR** (150 MHz, CDCl$_3$): δ = 171.05, 164.14, 151.48, 145.84, 140.87, 140.36, 140.28, 137.74, 137.43, 137.04, 135.43, 135.00, 132.57, 132.34, 132.28, 132.23, 132.10, 132.04, 131.96, 131.89, 131.66, 131.16, 130.87, 130.65, 130.40, 130.35, 129.58, 129.23, 129.13, 129.05, 128.98, 128.73, 127.54, 127.05, 126.99, 126.86, 126.61, 126.51, 124.31, 124.24, 124.17, 124.12, 123.60, 123.07, 122.79, 121.10, 121.05, 120.57, 120.39, 84.09, 32.05, 30.84, 30.67, 29.84, 29.79, 29.73, 29.60, 29.48, 29.44, 29.29, 24.16, 22.84, 14.29. **ESI-MS** calculated for $C_{110}H_{117}N_2O_6S_6^-$ [M−H]$^-$ 1754.73, found:1754.52.

2.18. 5,5'''''-dibromo-3,3'''',3''''',4'-tetraoctyl-2,2':5',2'':5'',2''':5''',2'''':5'''',2'''''-sexithiophene (BB)

In a flask containing 1.05 g (1.06 mmol) of **10** in 15 mL of a 1:1(v/v) mixture of chloroform - acetic acid, 0.41 g (2.3 mmol) of N-bromosuccinimide (NBS) were added in small portions at 0 °C, under stirring and nitrogen flow. The reaction is maintained at room temperature overnight. The reaction was quenched by addition of water and the mixture was extracted with CH$_2$Cl$_2$. The organic layers were washed with a saturated solution of NaHCO$_3$ (three times), water and brine and dried with anhydrous Na$_2$SO$_4$. After filtration and solvents removal, the crude product was purified by flash column chromatography using petroleum ether as eluent and the final product **BB** was obtained as a dark orange/red solid (1.04 g, 89 %). **^{1}H NMR** (600 MHz, CDCl$_3$): δ = 7.14 (d, J = 3.7 Hz, 2H), 7.04 (d, J = 3.7 Hz, 2H), 6.89–6.88 (m, 4H), 2.77 (app. t, J = 7.8 Hz, 4H), 2.71 (app. t, J = 7.8 Hz, 4H), 1.67 (quint, J = 7.5 Hz, 4H), 1.61 (quint, J = 7.5 Hz, 4H), 1.30 (m, 40H), 0.88 (app. t, J = 7.0 Hz, 12H); **^{13}C NMR** (150 MHz, CDCl$_3$): δ = 140.43, 140.22, 137.00, 134.93, 133.11, 132.88, 132.06, 130.81, 129.25, 126.66, 124.12, 110.52, 32.04, 30.69, 30.66, 29.68, 29.57, 29.53, 29.51, 29.42, 29.40, 29.37, 22.83, 14.28.

2.19. Tetra-tert-butyl 4,4',4'',4'''-(((3,3'''',3''''',4'-tetraoctyl-[2,2':5',2'':5'',2''':5''',2'''':5'''',2'''''-sexithiophene]-5,5'''''-diyl)bis(4,1-phenylene))bis(azanetriyl))tetrabenzoate (CBBC)

100 mg (0.177 mmol) of block **C** and 75 mg (0.068 mmol) of **BB** were dissolved in 5 mL of dimethoxyethane (DME) and the solution was carefully degassed. Then, 354 μL (0.708 mmol) of a 2 M tripotassium phosphate solution were added. After further degassing, 16 mg (0.017 mmol) of $Pd_2(dba)_3$ and 10 mg (0.034 mmol) of $[HP(t-Bu)_3]BF_4$ were added and the resulting suspension was stirred at room temperature for 24 h. After the reaction was completed, it was poured into water and it was extracted with dichloromethane. The organic phases were dried with sodium sulfate and, after the solvent removal, the crude product was used without further purification. **CBBC** yield was calculated at ^{1}HNMR and resulted in 71 %. **^{1}H NMR** (400 MHz, CDCl$_3$): δ = 7.90 (d, J = 8.8 Hz, 8H), 7.53 (d, J = 8.5 Hz, 4H), 7.15–7.10 (m, 16H), 7.08 (s, 2H), 7.01 (s, 2H), 2.81 (m, 8H), 1.71 (quint, J = 7.5 Hz, 8H), 1.60 (s, 36H), 1.30 (m, 40H), 0.88 (app. t, J = 6.8 Hz, 12H); **^{13}C NMR** (100 MHz, CDCl$_3$): δ = 165.44, 150.54, 145.62, 141.02, 140.79, 140.20, 136.84, 135.10, 134.34, 130.99, 130.67, 130.28, 130.13, 128.63, 126.78, 126.50, 126.44, 126.17, 124.05, 122.83, 80.87, 32.24, 32.21, 32.02, 30.68, 30.64, 29.70, 29.56, 29.41, 28.35, 22.81, 14.26.

2.20. 4,4',4'',4'''-(((3,3'''',3''''',4'-tetraoctyl-[2,2':5',2'':5'',2''':5''',2'''':5'''',2'''''-sexithiophene]-5,5'''''-diyl)bis(4,1-phenylene))bis(azanetriyl))tetrabenzoic acid (D6D)

60 mg (0.033 mmol) of **CBBC** were dissolved in 1 mL of CH$_2$Cl$_2$. Next, 0.2 mL of trifluoroacetic acid were added. The resulting solution was stirred at room temperature for 6 h. After the solvent removal, the final product **D6D** was obtained quantitatively, as an orange solid (53 mg, quantitative). **^{1}H NMR** (600 MHz, THF-d8): δ = 7.93 (d, J = 8,9 Hz, 8H), 7.63 (d, J = 8.7 Hz, 4H), 7.31 (s, 2H), 7.25 (d, J = 3.8 Hz, 2H), 7.17 (d, J = 8.7 Hz, 4H), 7.15–7.13 (m, 10*H*), 7.09 (s, 2H), 2.85 (app. t, J = 7.7 Hz, 8H), 1.45 (m, 8H), 1.30 (m, 40H), 0.89 (app. dt, J = 7.0 Hz, 12H). **^{13}C NMR** (150 MHz, THF-d8) δ = 167.23, 151.77, 151.53, 146.96, 142.27, 141.82, 141.26, 137.79, 135.97, 135.47, 132.17, 131.78, 131.15, 130.83, 129.67, 127.65, 127.45, 127.32, 126.52, 125.25, 123.78, 33.07, 33.06, 31.62, 31.61, 30.81, 30.65, 30.61, 30.59, 30.55, 30.45, 30.44, 30.35, 23.75, 14.65. **ESI-MS** calculated for $C_{96}H_{103}NO_8S_6^-$ [M−H]$^-$ 1604.61 (100 %) and 1603.60 (94.9 %) found:1604.52 (100 %) and 1603.23 (93.8 %).

2.21. Computational investigation of selected dyes

The ground-state electronic structure of the dye **A6D** here considered was investigated with a density functional theory (DFT) approach, similar to what has been adopted for the analysis of **P1** dye-sensitizer in a previous work from us [52]. The excited state and the absorption spectrum were simulated in the framework of linear-response time dependent DFT (LR-TDDFT) theory. A series of hybrid functions, differing by the Hartree–Fock exchange percentage, were considered in the initial phase, aiming at identifying the method capable of

reproducing the experimental UV–vis spectrum with greatest accuracy. The performance was evaluated through the calculation of the average difference between calculated and experimental absorption wavelengths of the three transitions reported in the spectrum (Fig. A1), namely 524, 427 and 352 nm for **A6D**. It is important to underline at this stage that

the choice of different benchmarks, for instance the HOMO energy level of the ground state obtained from voltammetry studies, (see above) may lead to different scores. The following Density Functionals were tested: CAM-B3LYP [53], PBE0 [54,55] and M06-2X [56]; the polarized 6–31 + G(d,p) basis set was used in all models, and the presence of the solvent
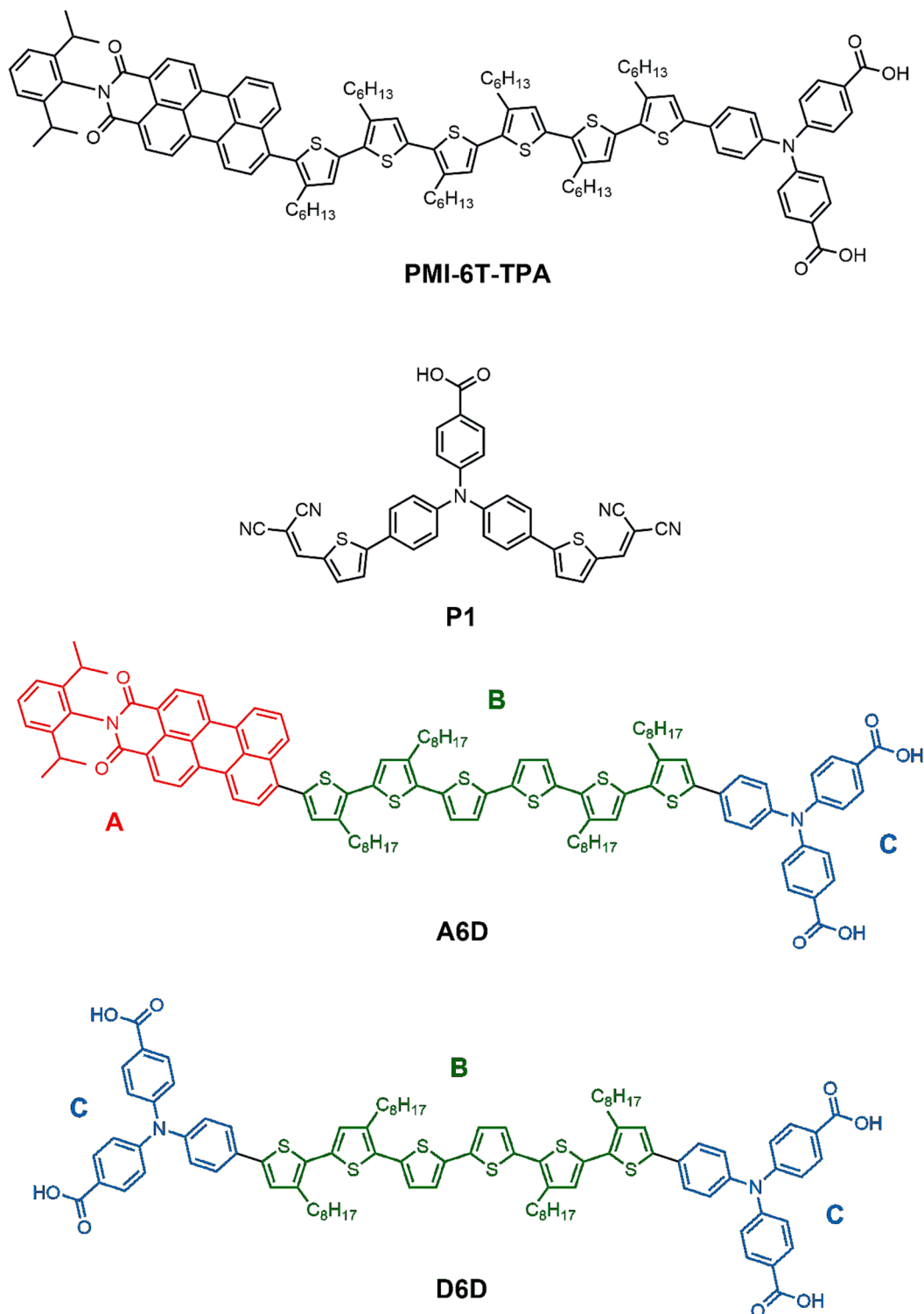
Fig. 2. Chemical structures of PMI-6T-TPA and P1 (as reference benchmarks) and the newly synthesized sensitizers **A6D** and **D6D** presented for the first time in this work. For sake of comparison the structure of **A6D** (Fig. 1) is here represented once again. Both **A6D** and **D6D** constitute multifunctional systems since they can be viewed as assemblies of blocks with different functions. The blocks having different functions have been coloured according to the colour code specified in the caption of Fig. 1: in red the acceptor unit PMI, in green the oligothiophene bridging π-spacer and in blue the donor moiety TPA. The donor block contains the anchoring carboxylic functions.

(acetonitrile) was taken into account using the Polarizable Continuum Model (PCM) formalism (IEF variant, as implemented in the code Gaussian) with 35.688000 and 1.806874 as static and infinite frequency dielectric permittivity values, respectively.

2.22. Device component preparation and cell assembly and characterization

Fluorine-doped tin oxide (FTO)-coated glasses (15 Ω sq^{-1}, Sigma Aldrich) were washed with water and detergent, then with ethanol, and finally dried with compressed air. NiO$_x$ photoelectrodes were prepared as reported elsewhere[46]. Sensitization process of the prepared NiO$_x$ electrodes was made using a 0.2 mM solution of each dye in DMF. Photocathodes were activated using a plate at 100 °C for 20 min, then they were dipped, still hot, in the dye solution in darkness condition. After 3 h of dyeing, the sensitized electrodes were rinsed in anhydrous DMF to remove the physisorbed dye and dried in air on filter paper to remove any traces of solvent. Counter-electrodes were made by spreading a 5 mM H$_2$PtCl$_6$ solution in propan-2-ol on FTO glass, followed by a heating step at 400 °C for 30 min on a heating plate and then let slowly cooled down to RT. Electrolyte was prepared by dissolving 1.34 g of LiI, 0.077 g of I$_2$ and 2.52 g of 1-methyl-3-propyl imidazolium iodide in a mixture of acetonitrile/valeronitrile (85: 15) to obtain a 0.9 M and 0.1 M solution of I$^-$ and I$_3^-$ in ACN. Dye-sensitized photocathodes and counter-electrode were pressed together (90 °C for 15 s each side) by means of a thermoplastic polymer gasket by Surlyn®. Then, the electrolyte is inserted into the cell by back-vacuum filling technique from a channel in the thermoplastic gasket. The channel was then closed with a commercial bi-component epoxy resin. The active area of the resulting devices is 0.25 cm^2.

Devices performances were tested by using a solar simulator (model 10500, ABET Technologies Inc.) under 1 sun light illumination (xenon arc lamp of 150 W) connected to a Keithley multimeter (SMU 2420, Tektronix, USA), and calibrated by a silicon reference solar cell (irradiation sensor, Spektron 210). Incident photon-to-current conversion efficiency and light intensity-dependent measurements were performed with an all-in-one platform (ARKEO - Cicci Research s.r.l.) composed by a Xenon based monochromatic line (double grating with range of 300–1100 nm), a LED-based bias light, thermal stage, and 4-wire source meter unit. The external quantum efficiency (EQE) was acquired with digital lock-in demodulation at a chopping frequency of (13 Hz). JV curves were recorded in forward scan, *i.e.* modulating the voltage from 0 V (short-circuit) to the maximum value corresponding to open-circuit at the scan rate of 20 mV s^{-1}. JV curves were acquired ramping automatically the light from 0.1 to 1 SUN of equivalent intensity.

Stability tests were performed by storing the cells at RT and in dark condition. The JV curves were recorded at fixed time intervals. Transmittance of complete devices were measured with a UV–vis spectrophotometer (Varian Cary 300 Bio, Agilent technologies) in the double beam mode using air as blank.

3. Results and discussion

Fig. 2 shows in a comparative way the chemical structures of the dyes employed throughout this paper. As reported in the introduction, **PMI-6T-TPA** and **P1** are the current state-of-art and the most common sensitizer for *p*-DSCs. The newly synthetized dyes are named **A6D** and **D6D** to evidence the asymmetric pattern of the type A-π-D in the former and the symmetric D-π-D structure of the latter.

3.1. Synthesis of A6D

The synthetic strategy at the basis of **A6D** and **A6A** preparations foresees a convergent synthesis. The molecule was divided into three main functional blocks (Blocks A, B and C) that were synthesized separately and then reacted to give the final product (Schemes 1-5). The
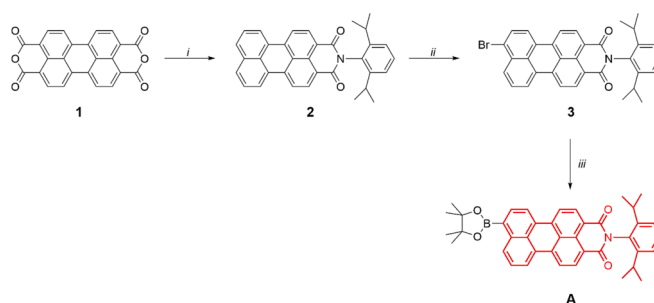
Scheme 1. Synthesis of block A. Reaction conditions: (i) 2,6-diisopropylaniline, zinc acetate, imidazole, water, 180 °C; (ii) Br$_2$, CH$_2$Cl$_2$, reflux; (iii) bis (pinacolato)diboron, Pd(dppf)Cl$_2$, potassium acetate, dioxane, 90 °C.

chance to design a convergent synthesis has several advantages over a linear one: it allows to intervene chemically on individual blocks with possibility of making small changes separately on the single blocks in a much simpler way with respect to the approach that considers changes only on the entire combined structure, a system that is constitutionally less workable and harder to process. In the convergent approach the properties of a single block are easily modulated and it can be studied how these changes made on single block affect the properties of the entire combined molecule, *i.e.* the multiblock synthetic target. In addition, the division into blocks and their subsequent coupling allows us to synthesize sister molecules by replacing a single block. To design push–pull dyes, these advantageous aspects are very important, because the modification of a single moiety could affect dramatically the performance of the combined molecule in its performance as sensitizer in the DSC.
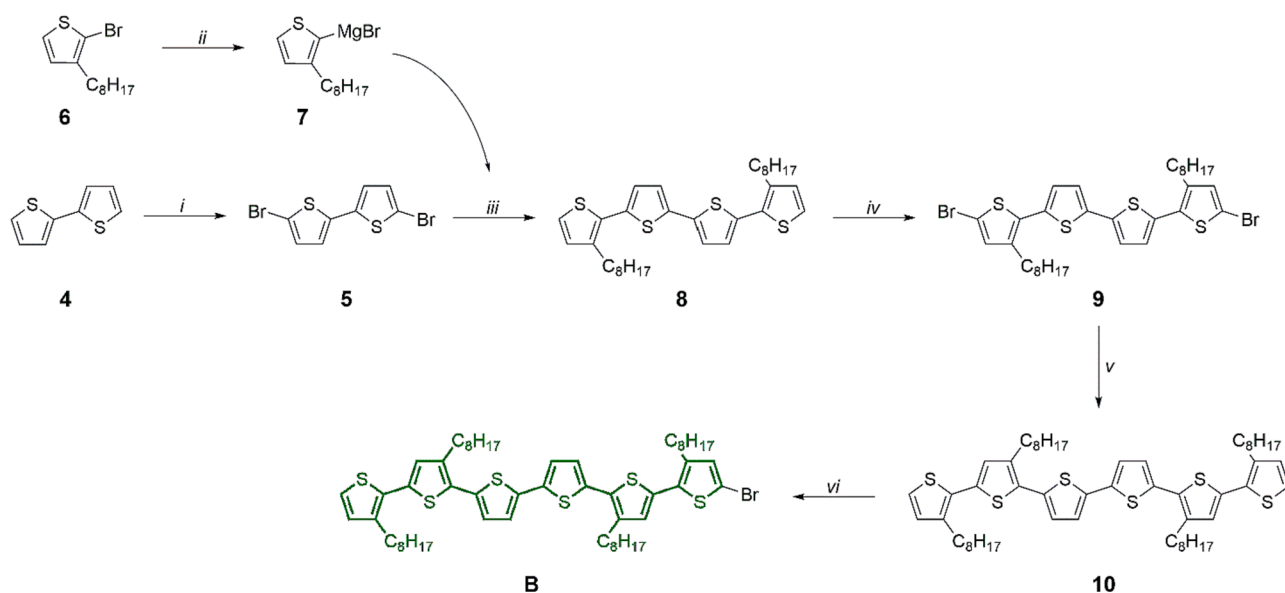
3.2. Synthesis of block a

Scheme 1 shows the synthetic route to obtain *N*-(2,6-diisopropylphenyl)-9-(4,4,5,5-tetramethyl-[1–3]dioxaborolan-2-yl)perylen-3,4-dicarboxymide (**A**). The first step is the synthesis of *N*-(2,6-diisopropylphenyl)perylene-3,4-dicarboxymide (**2**) obtained in autoclave [57] by reacting a mixture of perylene-3,4,9,10-tetracarboxilic dianhydride (**1**), 2,6-Diisopropylaniline, zinc acetate dihydrate, imidazole and water at 180 °C for 24 h. The second step is the bromination of compound **2** with molecular bromine at room temperature using dichloromethane as the solvent. From the obtained brominated product **3**, it is possible to obtain the compound **A** by a palladium-catalyzed Miyaura boronation reaction, carried out at 90 °C in dioxane, using Pd(dppf)Cl$_2$ as the catalyst, bis(pinacolato)diboron as a boronation agent and potassium acetate as a base. The base was potassium acetate (AcOK) because, in general, the use of stronger bases, such as potassium carbonate (K$_2$CO$_3$) or potassium phosphate (K$_3$PO$_4$), can promote the side reaction between the forming organo-boron product **A** and the brominated starting reagent **3**, resulting in the formation of the aryl coupling product (Suzuki-Miyaura cross-coupling) [58].
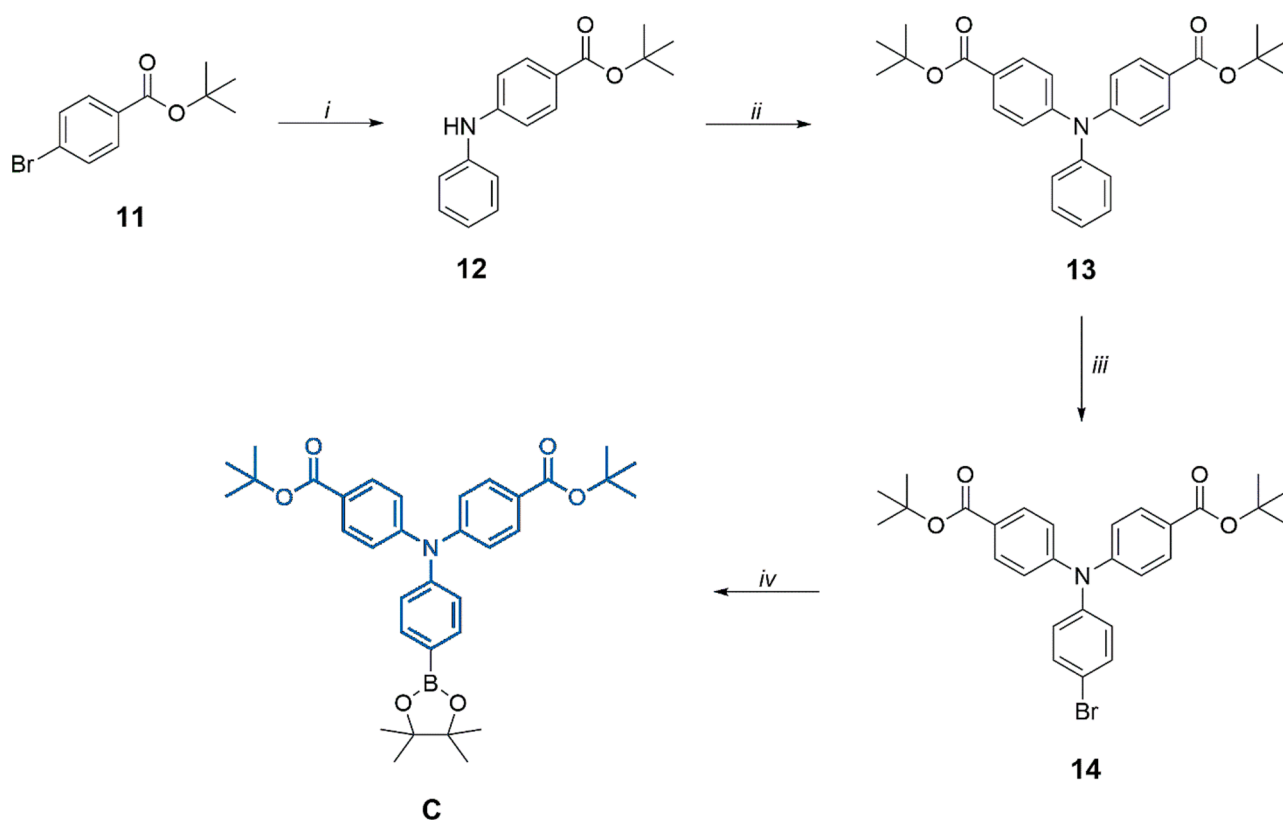
3.3. Synthesis of block B

The synthetic route depicted in Scheme 2 concerns the synthesis of 5-bromo-3,3′′′,3′′′′′,4′-tetraoctyl-2,2′:5′,2′′:5′′:5′′′,2′′′′:5′′′′,2′′′′′-sexithiophene (**B**). The first step consists in the bromination of the oligothiophene core (*i.e.*, 2,2′-bithiophene **4**). The brominated bithiophene **5**, obtained in quantitative yield, was then used in a Kumada coupling reaction with the already synthesized Grignard reagent 3-octyl-2-thienylmagnesium bromide **7** to obtain 3,3′′′-dioctyl-2,2′:5′,2′′:5′′,2′′′-quaterthiophene **8** with a 76 % yield. The Kumada reaction was catalyzed by Ni (dppp)Cl$_2$, a nickel-phosphine complex, because it was easy to synthesize and particularly effective in reactions involving Grignard reagents [59]. In the following step, the newly obtained product **8** was

Scheme 2. Synthesis of block B. Reaction conditions: (i) NBS, CHCl₃/AcOH, rT; (ii) Mg, 1,2-dibromoethane, Et₂O, reflux; (iii) 3-octyl-2-thienylmagnesium bromide (**5**), Ni(dppp)Cl₂, Et₂O, reflux; (iv) NBS, CHCl₃/AcOH, rT; (v) 3-octyl-2-thienylmagnesium bromide (**5**), Ni(dppp)Cl₂, Et₂O, reflux; (vi) NBS, CHCl₃/AcOH, rT.

Scheme 3. Synthesis of block C. Reaction conditions: (i) aniline, Pd₂(dba)₃, [HP(t-Bu)₃]BF₄, potassium *tert*-butylate, toluene, 40 °C; (ii) *tert*-butyl 4-bromobenzoate (**11**), Pd₂(dba)₃, [HP(t-Bu)₃]BF₄, potassium *tert*-butylate, toluene, 80 °C; (iii) NBS, DMF, rT; (iv) bis(pinacolato)diboron, Pd(dppf)Cl₂, potassium acetate, dioxane, 80 °C.

brominated again, under the same conditions as described above, to obtain the dibrominated compound 5,5‴-dibromo-3,3″-dioctyl-2,2′:5′,2′:5′,‴,2′′-quaterthiophene (**9**) quantitatively. The last two steps involved a further Kumada reaction to obtain sexithiophene **10**, followed by a monobromination reaction. To reduce the possibility of obtaining dibrominated product, small aliquots of brominating agent (NBS) were added during four hours at 0 °C. Block **B** was obtained after

purification with a 44 % yield.

3.4. Synthesis of block C

Synthesis of block C (Scheme 3) involves four steps: the first consists of a Buchwald-Hartwig amination reaction between *tert*-butyl 4-bromobenzoate **11** and aniline to obtain the coupling product, diphenylamine
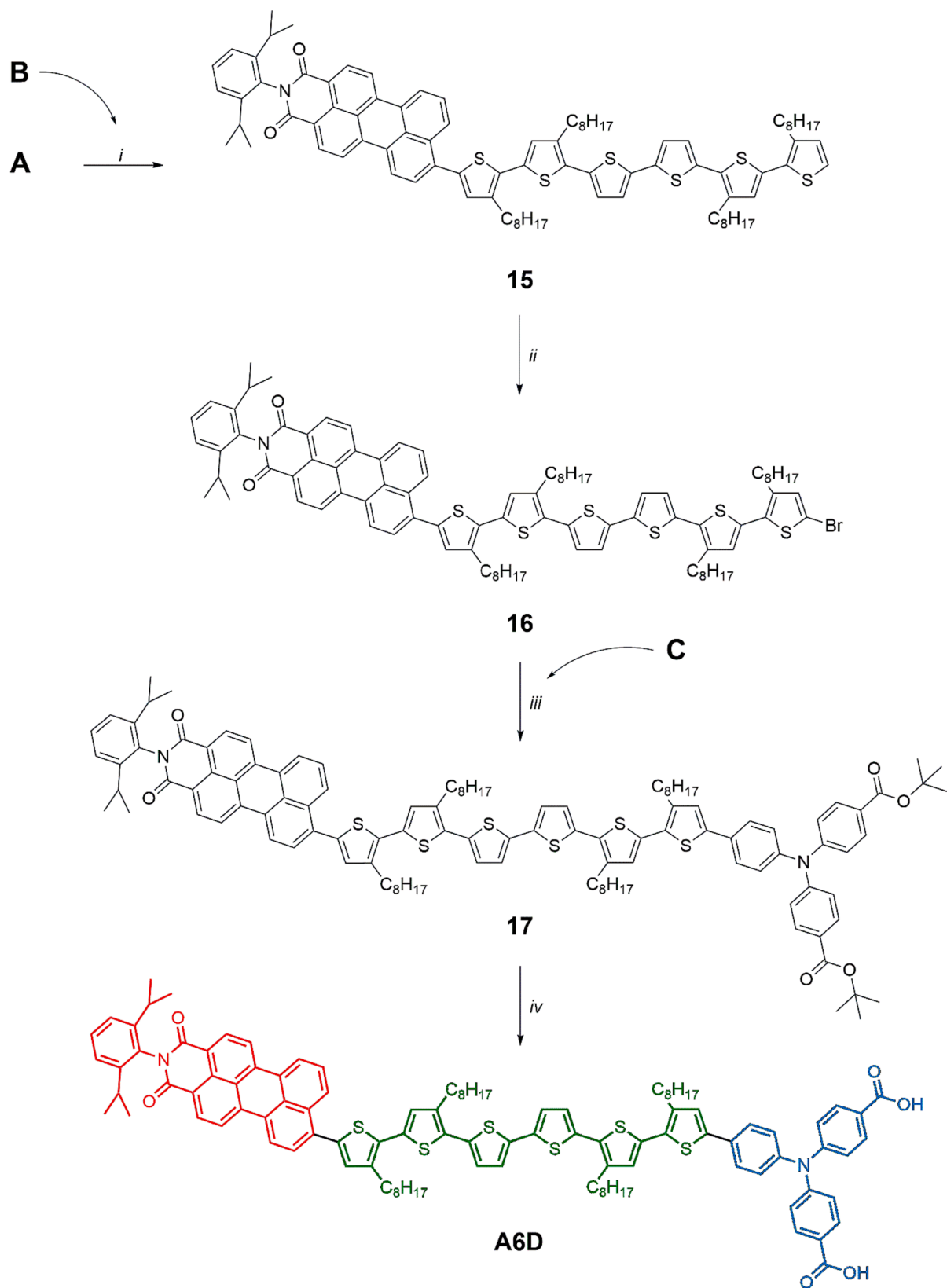
Scheme 4. Synthesis of A6D. Reaction conditions: (i) Pd$_2$(dba)$_3$, [HP(t-Bu)$_3$]BF$_4$, potassium phosphate solution (2 M), DME, rT; (ii) NBS, CHCl$_3$/AcOH, rT; (iii) Pd$_2$(dba)$_3$, [HP(t-Bu)$_3$]BF$_4$, potassium phosphate solution (2 M), DME, rT; (iv) trifluoroacetic acid, CH$_2$Cl$_2$, rT.
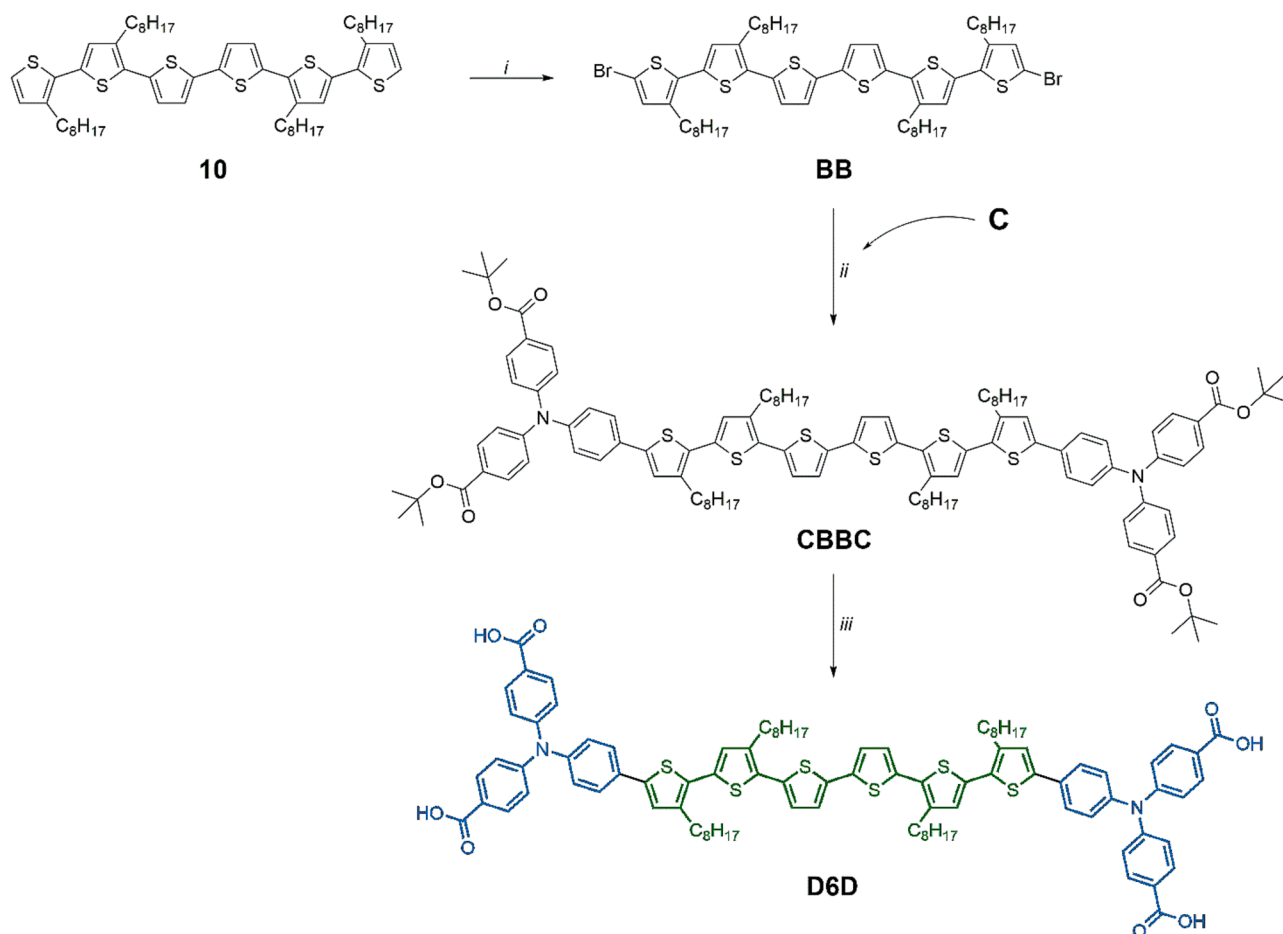
Scheme 5. (i) NBS, CHCl$_3$/AcOH, rT; (ii) Pd$_2$(dba)$_3$, [HP(t-Bu)$_3$]BF$_4$, potassium phosphate solution (2 M), DME, rT; (iii) trifluoroacetic acid, CH$_2$Cl$_2$, rT.

12. The subsequent step is the synthesis of triphenylamine **13** via another Buchwald-Hartwig reaction between *tert*-butyl ester **11** and diphenylamine **12.** Hartwig [60] and Buchwald [61] noted that the reductive elimination process of the organo-palladium complex is accelerated by the presence of trialkylphosphine ligands such as P(t-Bu)$_3$. In these syntheses, we have used trialkylphosphonium salts, such as [HP(t-Bu)$_3$]BF$_4$ instead of P(t-Bu)$_3$, because they are air-stable and easier to handle [62]. The subsequent bromination of compound **13** with *N*-bromosuccinimide (NBS) in dimethylformamide allowed us to obtain brominated triphenylamine **14** with a 77 % yield. In the final step, starting from brominated triphenylamine **14,** compound **C** was prepared by a palladium-catalyzed Miyaura boronation reaction, under the same conditions previously adopted.

3.5. Synthesis of A6D

Scheme 4 shows the reactions that lead to the attainment of the target molecule **A6D**. The first step consists of the union of block A with block B, through a Suzuki-Miyaura cross-coupling reaction, with formation of compound **15**. The reaction is carried out in dimethoxyethane at room temperature using the catalyst pair Pd$_2$(dba)$_3$ / [HP(t-Bu)$_3$]BF$_4$ and potassium phosphate as a base. The used catalytic system has been proved to be very active in these reactions since it can be obtained the aryl coupling product in excellent yields and in mild conditions [63]. The following step is the bromination of compound **15** with NBS in a 1:1 (v/v) chloroform / acetic acid solution to obtain compound **16** in quantitative yield. Subsequent Suzuki-coupling of brominated perylenyl-sexithiophene **16** and the boronic ester **C** led to perylenyl-sexithiophene-triphenylamine **17** in good yield (75 %). The reaction is

carried out in the same experimental conditions as described above. Then, compound **17** is subjected to a cleavage of both ester functions by acid hydrolysis with trifluoroacetic acid in dry dichloromethane at room temperature to give the carboxylic acid functions in **A6D** in quantitative yield.

3.6. Synthesis of D6D

The synthesis of the symmetrical dye **D6D** was designed by modifying the molecule **A6D** through the replacement of the electron withdrawing group (PMI, block A) with block C (Scheme 3). The latter block consists of the triphenylamine donor bearing two anchoring carboxyl groups. In this context, the aim is to investigate the effects two donor symmetrical groups connected to a π-bridge, exert on electronic transfer. The symmetry of this molecule allowed us to reduce the final steps to a single Suzuki-coupling.

The synthetic route depicted in Scheme 5 concerns the synthesis of 4,4′,4′′,4′′′-(((3,3′′′′,3′′′′′,4′-tetraoctyl-[2,2′:5′,2′′:5′′,2′′′:5′′′,2′′′′:5′′′′,2′′′′′-sexithiophene]-5,5′′′′′-diyl)bis(4,1-phenylene))bis(azanetriyl))tetrabenzoic acid (**D6D**). The first step consists in the bromination of the sexithiophene **10** using NBS as a brominating agent. The dibrominated sexithiophene BB has been reacted with the compound C in a Suzuki-Miyaura cross-coupling reaction, obtaining the compound CBBC. The reaction is carried out in dimethoxyethane at room temperature using the catalyst system Pd$_2$(dba)$_3$ / [HP(t-Bu)$_3$]BF$_4$ with a 71 % yield. The final acid hydrolysis of all ester functions, using trifluoroacetic acid in dry dichloromethane at room temperature, gave the tetracarboxylic acid **D6D** with a quantitative yield.

3.7. Conformational investigation of A6D

The careful design of **A6D** aims to the increase of coplanarity between adjacent functional blocks in comparison to the reference molecule **PMI-6T-TPA**: a more planar system is expected to lead to a widening of the absorption spectrum of the dye with inclusion of longer wavelengths of absorption with respect a non coplanar system of analogous extent [64]. This widening is dramatically important to extend the portion of the solar light absorbed by the dye, especially in the low-energy range (*i.e.* NIR and IR). In this context, we have considered a modification of the pattern of substitution of the oligothiophene-based central with alkyl chains on going from **PMI-6T-TPA** to the target molecule **A6D**: the number of the alkyl chains is reduced from six to four and their length increased from hexyl to octyl. More importantly, there also a change in the position of anchoring: alkyl chains are bound in positions 4′′′′, 4′′′′′ and 3′′′′, 3′′′′′ respectively in **PMI-6T-TPA** and **A6D** (Fig. 2, first and third structure). This modification aims at reducing the steric hindrance between the perylene block and the oligothiophene backbone with its side chains: in particular, the hexyl chain in position 4′′′′′ in **PMI-6T-TPA** is expected to hinder the free rotation of the bond between the perylene and the attached thiophene unit. This would lead to an increase of the dihedral angle between the two aromatic systems, and hampers the planarity of the whole system. The latter conformational feature is desirable to achieve a sizeable electron conjugation. On the contrary, in **A6D**, the alkyl chain located in position 3′′′′′ is expected not to have a significative impact on the freedom of movement between the two connected aromatic systems. It is likely that this structural feature leads to the reach of a smaller dihedral angle (tending to 0°) between the perylene plane and that of the thiophene units. This would impart a quasi-flat conformation for the target molecule [65]. In order to support this hypothesis, we performed calculations using CAM-B3LYP and M06 density functional theory methods (see experimental section for further details). For sake of simplicity without reducing the meaningfulness of the calculation, two model systems of minor complexity and with a smaller number of atoms with respect to **A6D** and **PMI-6T-TPA** have been chosen (Fig. 3). These consist in two small fragments of **A6D** and **PMI-6T-TPA**, which contain the perylene block connected to two thiophene rings. The bithiophene block is differently substituted in the two model systems A6D-h3 (Fig. 3b) and A6D-h4 (Fig. 3a), representative of **A6D** and **PMI-6T-TPA**, respectively. The alkyl substituents on the bithiophene unit are two hexyl groups. In A6D-h3 the hexyl groups are positioned in 3 and 4′ with respect to the 2,2′ bond connecting

the two thiophene units. In A6D-h4 the alkyl substituents are in the position 4 and 3′ with respect to the 2,2′ bond connecting the two thiophene units. The optimized geometries confirm that the arrangement of the proximal thiophene ring relative to the perylene moiety is different for the two configurations (Fig. 3a and 3b). Indeed, in the A6D-h4 model structure (configuration with the alkyl chain in position 4), the dihedral angle C (pery-non substituted)-C-C5(thio)-C4(thio) is −111.05°, whereas in the A6D-h3 structure (configuration with the alkyl chain in position 3) the dihedral angle is reduced to −49.65°, making this latter structure significantly closer to planarity.

Reported calculation have been also supported by experimental evidences collected by ^{1}H NMR. When the spectra of **A6D** and **PMI-6T-TPA** are compared, it is observed a difference in the chemical shift of perylene proton H8. Such a signal is diagnostic of the conformation assumed by the perylene block with respect to the thiophene units [66]. In **PMI-6T-TPA**, H8 signal is located at 8.06–8.00 ppm [67] and appears as a multiplet corresponding to five protons (four aromatic protons in ortho positions to the carboxyl functions and proton H8 of perylene). This signal is more shielded than the proton H8 of **A6D**, which appears at 8.54–8.47 ppm in a multiplet together with four other perylene protons (H2, H5, H7, H12). The "ring-current effect" [68] would explain the de-shielding experienced by proton H8 in **A6D**. The reduction of the number of alkyl chain in **A6D** could result in a lower solubility of the dye-sensitizer with respect to **PMI-6T-TPA** in the most common apolar organic solvents (e.g. DMF, used for the dipping sensitization, *vide infra*). For this reason, the design of **A6D** molecular structure had considered the increase of alkyl chains length, from hexyl to octyl. In conclusion, the combination of the designed structural features in **A6D** allows an increased conjugation between the acceptor group (peryleneimide, PMI) and the oligothiophene chain, and warrants a major conformational freedom of the thiophene units which, in turn, can generate a more coplanar structure. The latter characteristic leads to an enhancement of π–system conjugation. As recently proved by some of us, conformational aspects play a significant role both in terms of dye absorption capabilities and HOMO energy modulation [69,70].

3.8. Computational analyses of A6D and D6D

A computational analysis of the electronic transitions of the target compounds **A6D** and **A6A** (Figs. A1 and A2) has been carried out to understand the origin of the observed spectra. The transition energies have been computed using the time-dependent DFT methodology (TD-
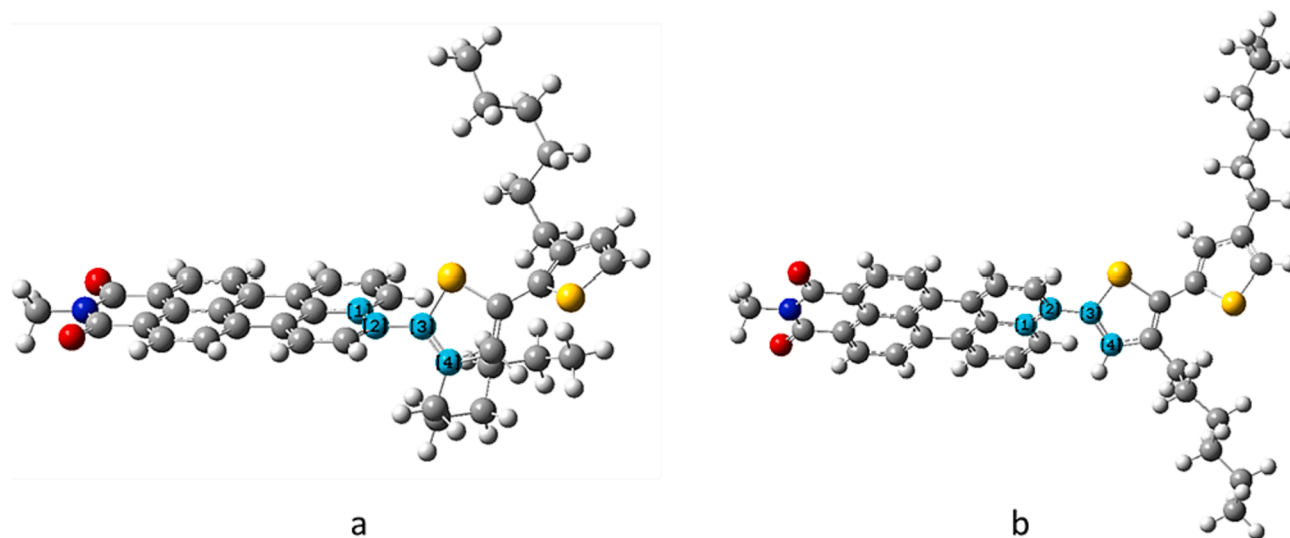

Fig. 3. Optimized geometries of A6D-h4 (left) and A6D-h3 (right) here considered as equivalent models for **PMI-6T-TPA** and **A6D**, refalysis of structural stability. The dihedral angle of interest is the one formed by the plane containing atoms 1–2–3 (evidenced in cyan) and the plane containing atoms 2–3-4 (evidenced in cyan).

DFT) using the PBE0, CAM-B3LYP and M06 hybrid functionals for a better assessment of the quality of the computations. A detailed comparison between the computed and experimental spectra of **A6D** is reported below. Our results show that the PBE0 functional performs rather poorly with a lower transition energy at 591 nm, which is about 0.27 eV lower in energy compared to the experimental value. Both CAM-B3LYP and M06 models provide more accurate results, and since among the twenty electronic transitions that have been calculated, (Table A1), those having the largest intensity (*i.e.* corresponding to transitions with larger oscillator strength) are in good agreement nicely with the positions of the three experimental peaks at 524, 427 and 362 nm (Fig. A1). In particular, the simulated spectrum obtained with the M06 provides the best results. The calculated (calc.) values of first two transition wavelength, 519 nm and 439 nm, deviate by at most 0.08 eV from the experimental values of 524 nm and 427 nm (see Table A1). Considering the good performance of the PCM/M06/6–31 + G(d,p) methodology, the same approach has been used to investigate the electronic properties of **D6D** as well (Table A2). The lowest energy peak predicted at 429 nm is only 0.03 eV blue-shifted with respect to the experimental value of 433 nm. The two calculated spectra (Figs. A1 and A2) were generated through the convolution of the various peaks, assigning a value of half width at half height (HWHH) of 0.15 eV to each spectral line. This choice allows the experimental and theoretical spectra to reach approximately the same upper wavelength limit of absorption and to justify the observed absorption broadening. The good results obtained made us confident that the calculations could be used to gain deeper insights into the relation between the structure and the electronic properties of the dyes. In the optimized geometries of the target compounds **A6D** and **D6D** (Figs. S3 and S4), there are different torsional arrangements for the thiophene rings. In particular, in **A6D** the dihedral angles corresponding to the single bonds joining the thiophene rings tend to arrange with a more planar configuration with respect to **D6D**. In moving from the perylene fragment of the PMI block to the phenyl group of TPA which is attached to the thiophene ring, the dihedral sequence is 134.65°-170.78°-154.48°-161.85°-153.16°-160.84°-154.80° in **A6D** and 155.29°-154.52°-153.20°-157.51°-153.19°-154.47°-155.29° in **D6D**. Therefore, the symmetric molecule **D6D** shows a more coil-like geometry. The comparison of the geometries of the frontier orbitals calculated for the two target systems show important differences (Fig. 4): the electron density of both HOMO and LUMO is concentrated in the central part of the symmetrical molecule in **D6D**, *i. e.* around thiophene rings (Figs. 4a and 4b), whereas in **A6D** the HOMO density is concentrated over and below thiophene rings and is practically absent around perylene and amine moieties (Fig. 4c). The LUMO density is spread over perylene rings of **A6D**, with no traces around thiophene rings and amine (Fig. 4d). This observation is in accordance with the variation of the total electron density (calculated over all molecular orbitals and not only over the frontier ones), when passing from the ground state (GS) to the excited state (ES). For **A6D** (Fig. A3) the density difference shows a marked depletion (cyan lobes) around thiophene rings and a parallel accumulation (purple lobes) in the perylene fragment. In **D6D** (Fig. A4) the electron density variations are mostly concentrated in the central portion and can be described as a rearrangement of the density among adjacent bonds. This trend complies well with the calculated values of total dipole moment of GS and ES, as reported in Table A3. Indeed, in **A6D** the dipole moment increases from 7.44 D to 18.30 D, with the vector lying on the line joining the central thiophene ring and the perylene system. In **D6D** the dipole moment decreases from 6.24 (GS) to 2.89 (ES) and is directed along the normal to the central thiophene ring. Overall, the perylene fragment acts as a strong attractor and pulls the electron density towards itself. Such a behaviour is desirable since it avoids charge concentration close in excess to the electrode surface. The latter phenomenon can promote unwanted recombination reactions leading to the binding of the photogenerated exciton [71,72]. Concerning the HOMO and LUMO energies (Table 1), it is found that HOMO energies are similar for **A6D** and **D6D** while LUMO energies differ of

approximately by 1 eV, with **D6D** displaying the highest value. The corresponding HOMO-LUMO difference is 3.69 eV in **A6D** and 4.71 eV in **D6D**. The larger gap found in symmetrical **D6D** is in accordance with the wavelength differences of the lowest energy transitions observed in the experimental UV–vis spectra of the two target compounds and the corresponding values calculated with TD-DFT. The lowest energy transitions have a systematically smaller gap than the HOMO-LUMO energy difference calculated for the ground state (corresponding to fundamental bandgap, E_g). The fundamental bandgap can be considered as equivalent to the difference between the energies of the first ionization potential and the first electron affinity (EA) the difference being probably due to excitonic binding energies, as reported by some authors [73–76]. According to TD-DFT treatment, the lowest energy transition of **A6D** cannot be straightforwardly described in terms of the HOMO-LUMO transition, but should be rather regarded as a combination of HOMO(-n)-LUMO transitions, with n varying between 0 and 3, for the strong electronic coupling between the different blocks. The different weight of the various HOMO(-n)-LUMO transitions is expressed in terms of the following percentages: 22 % for HOMO->LUMO, 39 % for HOMO(-1)->LUMO, 30 % for HOMO(-2)->LUMO, 5 % for HOMO(-3)->LUMO. accounting for a strong electronic coupling of the different blocks. The computed main transition in **D6D** has a different composition: 75 % HOMO->LUMO process, 10 % HOMO(-1)->LUMO and 3 % HOMO(-2)->LUMO. Such an outcome is expected for the "electronic insulation" of the central oligothiophene block from the two side triphenylamine units that act as moieties blocking conjugation. A confirmation of that is given by the verification that both HOMO and LUMO appear strongly localized in the oligothiophene unit (Fig. 4a and 4b).

As a consequence of the computed geometries of the frontier orbitals (Fig. 4), it has to be expected that the occurrence of the HOMO-LUMO transition in **A6D** brings about a displacement of the electronic cloud from the oligothiophene central block (Fig. 4c) to the electron accepting block PMI (Fig. 4d). This does not represent the case of **D6D** for which the occurrence of the HOMO-LUMO transition does not involve any significant displacement of the electronic cloud. In **D6D** the electronic cloud remains actually localized in the central oligothiophene block upon occurrence of the HOMO-LUMO transition (Figs 4a and 4b).

The observed behaviour of charge density and dipole moment shift between ground and excited state, just outlined for **A6D** and **D6D**, can be pointed out also in the small-scale models previously employed to confirm the planarity increase when going from **PMI-6T-TPA** to **A6D** as suggested by NMR experiments (namely A6D-h3 and A6D-h4 structures). Though not clearly visible in the HOMO, LUMO (Figs. A5–A8) as in the bigger molecules, the total density difference plots (Figs. A9 and A10) show a larger charge depletion in the first-neighbour thiophene ring (*i.e.* bigger cyan lobes at the same isodensity) when passing from GS to ES, in A6D-h3 than in A6D-h4; such an issue is further verified by the dipole moment changes (Table A4) that are +6.99 and +5.30 Debye for A6D-h3 and A6D-h4, respectively. The calculated TD-DFT spectra (Fig. A11) and ground-state HOMO and LUMO eigenvalues are in line with this hypothesis. The highest absorption wavelength, that is mainly described as a HOMO->LUMO transition, is redshifted by about 20 nm in **A6D**, and the HOMO-LUMO gap (Table A5) is smaller in **A6D** (4.23 eV *vs* 4.73 eV). Overall, our calculations suggest that the presence of a bithiophene moiety around the electron withdrawing group favours the charge transfer, that is more sizable when the substitution occurs at position 3 (farther from the perylene fragment), since in this case, owing to the smaller steric hindrance of the alkyl sidechains, a more planar arrangement, and consequently a better electron conjugation, can be achieved. In the full-sized dyes, the transfer effect is boosted when more thiophene rings are connected together (**A6D**),but disappears when the system is symmetric (**D6D**), because in this case the electron density remains confined in the central portion of the system.
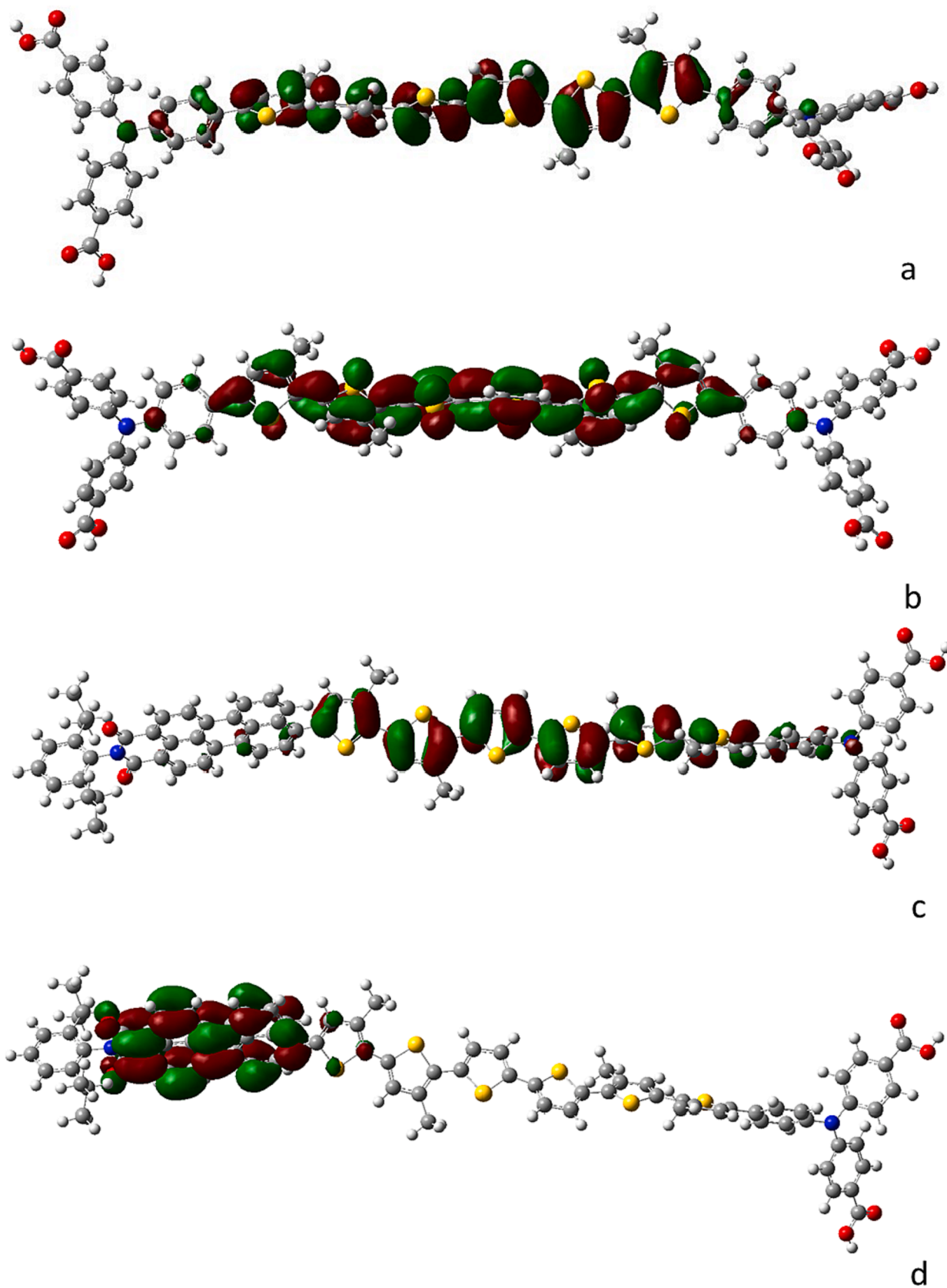
Fig. 4. Ground state HOMO and LUMO densities for **D6D** [(a): HOMO; (b): LUMO] and for **A6D** [(c): HOMO; (d): LUMO].

Table 1

Summary of key optical properties of **A6D** and **D6D**.

|	λ_{max}/ nm	(ε @ λ_{max})/M^{-1} cm^{-1}	Oxidation potential/eV	Reduction potential/eV	Optical (electrochemical) bandgap/eV	Ground state HOMO/eV (calc.)	Ground state LUMO/eV (calc.)
A6D	427, 524	43,899	−5.62 −5.85 −5.96	−3.77	2.23 (2.08)	−6.24	−2.55
D6D	433	56,252	−5.55 −5.80	–	2.38 (n.a.)	−6.27	−1.56

3.9. Spectroscopic characterization of A6D and D6

In order to be applied as sensitizer in *p*-DSCs, a dye should comply with some requirements: (i) it should have a HOMO level localized below the upper threshold of the valence band (VB) of the photocathode NiO$_x$, in order to allow an electron injection/hole extraction to/from the sensitizer/*p*-type semiconductor; (ii) it should have a LUMO level above the redox potential energy of the mediator (*i.e.* I$^-$/I$_3^-$) to warrant dye regeneration; (iii) it should show a relatively high molar absorption coefficient (ε) and a broad absorption spectra in order to harvest as many photons as possible from solar radiation. Absorption spectra of **A6D** and **D6D** are reported in Fig. 5a.

The calibration curves for the calculation of ε of the dyes in the sensitizing solution are reported in Fig. A12. **D6D** shows a slightly higher ε value (*i.e.* 5.6*10^4 M^{-1} cm^{-1} at λ_{max}) compared to **A6D** (ε = 4.4*10^4 M^{-1} cm^{-1} at λ_{max}). To determine the energy values of the frontier molecular orbitals, we adopted the combined electrochemical-spectroscopic approach. The HOMO level is related to the oxidation

potential of a given molecule, whereas the LUMO level is related to the reduction potential of the molecule [77]. In those cases, in which HOMO or LUMO could not be electrochemically evaluated (e.g. for problems of electrochemical stability of the electrolyte or lack of reversibility of the oxidation/reduction waves) the combined approach allows the calculation, for example, of the LUMO level by adding the energy of the optical band-gap (extracted from absorption/emission spectra) to the HOMO energy that has been determined electrochemically. The cyclic voltammetries (CVs) of **D6D** and **A6D** are reported in Figs. A13 and A14, respectively. In Figs. A13 and A14 the grey profiles refer to the reversible CV of the reference couple Fc/Fc$^+$.

The oxidative wave of **A6D** CV (red profile of Fig. A13) shows three quasi-reversible oxidation peaks centered approximately at 0.52 V, 0.75 V and 0.86 V *vs* Fc/Fc$^+$. One should note that a specific assignment of a peak to a single energy level could be misleading considering the mixed transition evidenced by computational analyses. Tentatively, we can assign to HOMO the second oxidation peak at intermediate potential, characterized by the higher reversibility and associated with the energy
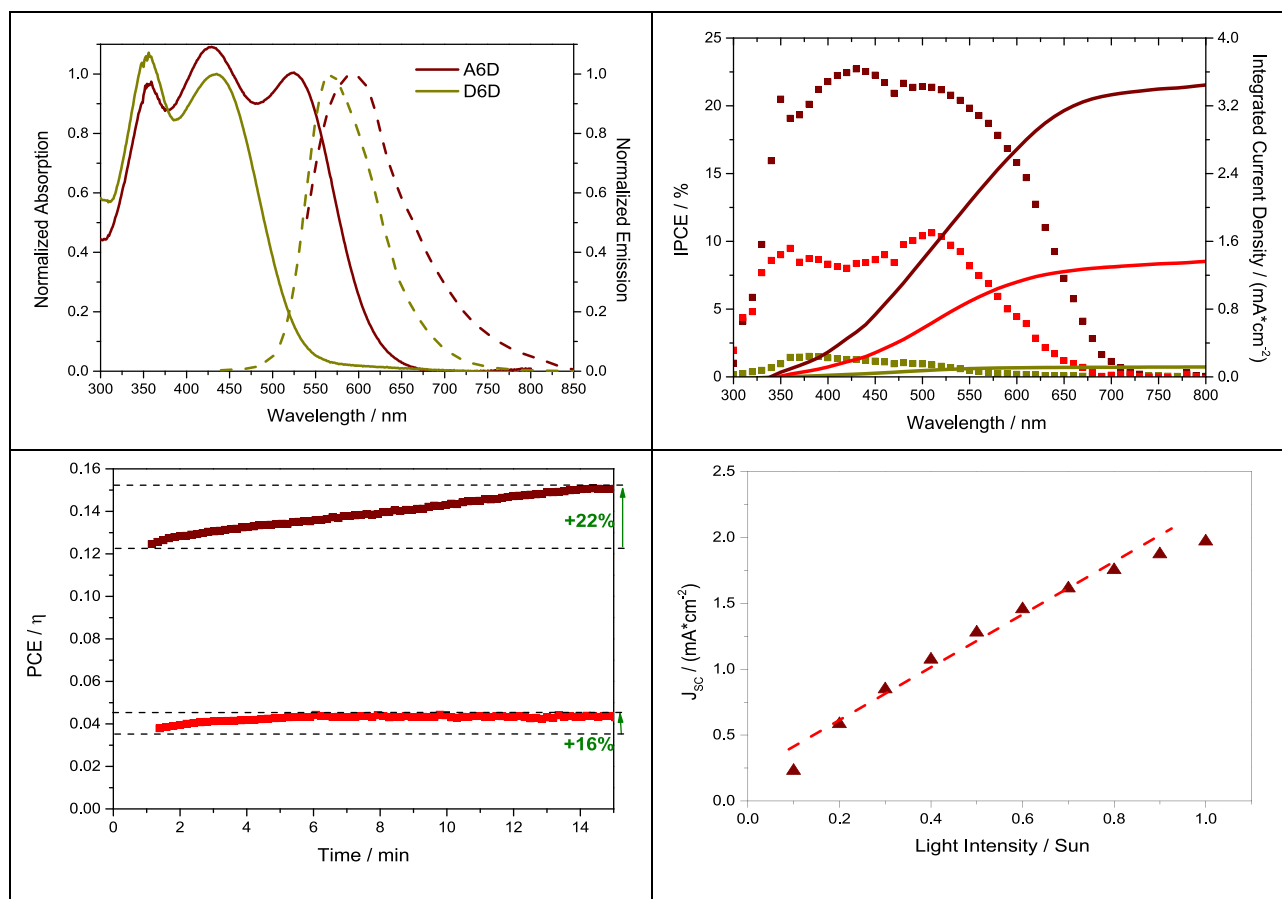
Fig. 5. Absorption (solid) and emission (dashed) spectra of **A6D** and **D6D** (a); IPCE spectra (dotted) and Integrated Current Density (solid) for devices assembled using **A6D**, **D6D** and **P1** (b); maximum power point (MPP) tracking of **A6D**- and **P1**-based DSSC (c); current density as a function of light intensity for **A6D**-sensitized DSSC (d). In all the frame the same colour code is used: **P1** in red, **A6D** in dark red and **D6D** in dark yellow.

level −5.85 eV *vs* vacuum. On the other hand, it is supposed that the first oxidation peak at the lower potential value is representative of the HOMO + 1 level and is associated to the value of absolute energy −5.62 eV *vs* vacuum (=zero energy level). Finally, the third oxidation peak at the highest potential value is associated with the energy level −5.96 eV *vs* vacuum and it is assigned to HOMO-1. The shoulder at about 0.25 V *vs* Fc/Fc⁺ is ill defined and is not taken into consideration in the present analysis. Given the relatively low value of oxidation potential it is believed that such a signal is associated to the oxidation of the electron-donating moiety of **A6D**, *i.e.* TPA which behaves electronically in an isolated manner for the scarce communication with the rest of the molecule (*vide supra*). In the reduction wave of of **A6D** (blue profile of Fig. A13) two irreversible current peaks are detected: the first at highest potential value has the onset at −1.33 V *vs* Fc/Fc⁺ (this corresponds to −3.77 eV *vs* vacuum) and is related to LUMO energy level. The second broad irreversible reduction peak is centered approximately at −1.83 eV and corresponds to −3.27 eV *vs* vacuum level. The irreversible signal at the lowest potential value is associated to LUMO + 1 of **A6D**. The electrochemical bandgap ($E_{g/ele}$) of **A6D** is calculated as the difference between HOMO and LUMO energy levels previously assigned from CV data. It is found $E_{g/ele}$(**A6D**) = 2.08 eV, a value which well matches with optical bandgap $E_{g/opt}$ = 2.23 eV. The latter value of $E_{g/opt}$ is obtained from the relationship

$$E_{g/opt}(eV) = 1240(nm{*}eV)/l_{a.e.}(nm) \tag{1}$$

in which $\lambda_{a.e.}$ represents the wavelength of the intercept between the absorption and the emission spectra. The latter is obtained as the wavelength at which the normalized spectra of absorption and emission spectra intersect [78].

The CV traces of **D6D** (Fig. A14) show in the oxidative wave (red profile) a broad shoulder below 0.45 V *vs* Fc/Fc⁺ and two well defined peaks (with reversible features) at about 0.55 and 0.80 V *vs* Fc/Fc⁺. In the reduction wave (blue profile) an irreversible signal is observed at −1.35 V *vs* Fc/Fc⁺. This is followed by a quasi-reversible wave at −1.95 V *vs* Fc/Fc⁺. The HOMO energy level could be estimated from electrochemical measurement and with corresponding value −5.80 eV *vs* vacuum level (with zero energy). The energy level of LUMO is estimated by subtracting the $E_{g/opt}$ (=2.38 eV) to the HOMO energy level. This results in the positioning of LUMO energy level at −3.42 eV *vs* vacuum level for **D6D**. All the values are summarized in Table 1. In the discussion of the electrochemical features of synthetized dyes, the possibility of having some peaks ascribable to SOMO (Single Occupied Molecular Orbitals) is not considered, because no evidence of unpaired electronic states could be extracted from DFT calculation. Moreover, the physical nature of the electronic state is expected to not modify sizeably the charge injection kinetics.

Both **A6D** and **D6D** dyes present HOMO energy levels lying below the upper threshold of NiO$_x$ VB, the latter being located at −5.1 eV *vs* vacuum. This feature allows an efficacious holes injection into the photocathode. At the same time, the LUMO energy level of both dyes is placed above the redox potential of the I-based mediator (*i.e.* −4.8 eV). This combination of features makes possible the exploitation of both dyes **A6D** and **D6D** as sensitizers for *p*-DSCs (*vide infra*).

3.10. Photovoltaic performances of A6D and D6D

The two newly synthesized molecules have been employed as dye-sensitizers in *p*-DSCs. The photoconversion performances of the corresponding devices are presented in Fig. 5b-d. The benchmark dye **P1** [40] was taken as reference due to its easiness of preparation and good photoelectrochemical efficiency.

As expected, **A6D**, due to its structural similarity with **PMI-6 T-TPA** [45], outperformed **P1** providing a more than double stabilized (*i.e.* after 1 month) PCE. The overall efficiency of the **A6D** based device reached a value of 0.087 % (Table 2). This is related to an increase of

Table 2
Photovoltaic figures of merit of champion DSSCs as a function of the ageing time. The tracking analyses of the device was made after 1000 h from devices assembly. Averaged values over 5 devices (for each dye) are reported in Table A6 with the associated statistical deviation.

Dye	Ageing time/η	V_{OC}/V	J_{SC}/mA*cm^{-2}	Fill Factor/%	PCE/%
P1	1	0.173	0.391	39.67	0.027
	24	0.175	0.459	38.73	0.031
	168	0.165	0.599	37.4	0.037
	672	0.151	0.662	36.88	0.037
	Before Tracking	0.103	1.005	36.23	0.037
	After Tracking	0.089	1.384	35.89	0.044
D6D	1	0.118	0.047	39.11	0.002
	24	0.122	0.089	42.22	0.005
	168	0.126	0.126	46.49	0.007
	672	0.112	0.115	46.32	0.006
A6D	1	0.214	0.403	44.85	0.039
	24	0.202	0.614	44.34	0.055
	168	0.200	0.831	39.84	0.066
	672	0.156	1.447	38.82	0.087
	Before Tracking	**0.136**	**2.529**	**36.39**	**0.125**
	After Tracking	**0.114**	**3.665**	**35.26**	**0.147**

photocurrent due to a minimization of recombination reactions. This is assured by the accurate design of **A6D** (*vide supra*). **A6D** showed a slow, constant increase of the photoconversion parameters with time whereas the efficiency of **P1**-based devices reached a plateau after 24 h. This could be related to the much bigger size of **A6D** with respect to **P1**, with **A6D**-modified surface requiring a longer time for the reach of optimized conditions of electrolyte wettability after the minimization of lateral interactions between adjacent anchored dye molecules. On the other hand, **D6D**-based devices showed poorer photoconversion performances with typical efficiencies below 0.01 %. This is ascribed to the localization of both the HOMO and LUMO on the π-spacer and consequent localization of the electronic wave in passing from the ground to a photoexcited state. This feature would favour the occurrence of recombination reactions (*vide infra*). The performances of the **P1**-based device here reported result lower when compared to what was recently published by some of us. This could be related to two different factors: (i) the absence of a blocking layer [41]; (ii) the use of a home-made electrolyte [79]; (iii) the smaller thickness of the electrode (1.5 μm) here adopted to improve the overall transmittance of the device (*vide infra*), which causes as drawback a lower dye-loading. The latter point is of particular interest considering a possible exploitation of DSCs in optically transmissive photovoltaics.

After the overall PCE is stabilized, we performed some MPPT (Maximum Power Point Tracking) analyses to investigate the behaviour of the two most performing cells under continuous light soaking. During the measurements, the cells are cooled with compressed air in order to avoid any effect of temperature increase. The latter effect might cause faster diffusion of the redox mediator with loss of meaningfulness in a comparative work of the photoelectrochemical properties.

Both **P1** and **A6D** devices (Fig. 5c) showed an amelioration of the photoconversion efficiency during tracking since the stabilized reached 0.044 % (+16 %) and 0.152 % (+22 %), respectively, after 15 min. The performances of **A6D**-based devices resulted the most stable ones since after tracking (see last line in Table 2), the current density was as high as 3.66 mA*cm^{-2} and the overall PCE was 0.147 %. It should be noted that compared to the PCE reported by Perera et al.[46] using a I-based electrolyte (0.60 %), our cells provide a four-fold lower efficiency (0.15 %). This could be mainly ascribed to the absence (in our devices) of both a blocking layer (BL) and the CDCA in the electrolyte. Indeed, BL and CDCA are expected to reduce the recombination reaction at the FTO/NiO$_x$ or FTO/electrolyte the former and at between the excited dye molecules the latter. As also proved by Perera et al.[46], a decrement around 40–50 % could be expected for a BL-free and CDCA-free devices. Moreover, the additional 30 % loss in PCE reported for our devices is

likely ascribable to the different thickness of the photoanode (*i.e.* 2 μm *vs* 4.2 μm), limiting the amount of dye loading and, thus, the J_{SC} of the DSSC.[42] In this context, the focus was the synthesis and characterization of the dyes and their proof-of-concept implementation in p-DSSCs.

For highlighting the contribution of different spectral regions to the overall powered current, the IPCE spectra of the differently sensitized devices were recorded. From the data reported in Fig. 5b, it emerges that the better conversion properties with **A6D** based devices were consequence of the improvement throughout the whole visible range (within which it falls IPCE$_{max}$ = 23 %) with inclusion of efficiency also the NIR region in comparison to **P1**, for which IPCE is null beyond 650 nm.

The better photoconversion performances of **A6D** devices compared to the **P1** ones are mainly related to the higher values of the short-circuit current density, J_{SC}. In the ambit of *p*-DSCs, it is well known that limitation in the current density is mainly ascribable to unwanted recombination reactions: the photoinjected holes react with an electron of the excited dye before being extracted to the external circuit, with consequent annihilation of the photogenerated exciton. The accurate design of a sensitizer with a LUMO located far away from the anchoring groups on TPA (and thus from the electrode surface), is of paramount importance to minimize recombination reactions. JV curves were recorded at different light intensity (from 0.1 to 1 Sun) for both **A6D** and **P1** based devices. The variation of the photovoltaic figures of merit as a function of light intensity are reported in Figs. A15 and A16 for **A6D** and **P1**, respectively. The analysis of J_{SC} behaviour in **A6D** devices (Fig. 5d) shows a quasi linear trend up to 0.9 Sun, an intensity value that once surpassed brings about a negative deviation. On the other hand, J_{SC} *vs* light intensity plot for **P1** devices deviates from linearity just above 0.4 Sun (Fig. A17), further proving the occurrence of more severe phenomena of recombination in **P1** devices compared to the ones with **A6D**, after the analyses of JV and IPCE data.

4. Conclusion

The present work has considered the realization of two new sensitizers for *p*-DSC application here indicated as **A6D** and **D6D**. These new dyes can be considered as constituted by three blocks having distinct function: an electron-accepting unit (peryleneimide, PMI), an electron-donating unit with electrode-anchoring carboxylic moieties (triphenylamine, TPA), and an oligothiophenic bridging block with an extended network of conjugated double bonds which warrant π-electrons delocalization, high electronic mobility and high electronic polarizability. **A6D** is a tri-block asymmetric structure of the type acceptor-π bridge-donator while **D6D** is a tri-block symmetric structure of the type donor-π bridge-donor. The design of **A6D** and **D6D** molecules was inspired by the *p*-DSC benchmark sensitiser **PMI-6 T-TPA** previously reported by Spiccia, Bach *et al.* Indeed, the state-of-the-art sensitizer **PMI-6 T-TPA** was modified with the realization of **A6D** and **D6D** for which the main structural differences with respect to **PMI-6 T-TPA** consisted in the variation of the number, relative position and length of the alkyl side chain constituting the substituents of the central oligothiophene core. The proposed structural changes realized in **A6D** and **D6D** ensured the planarity of these molecules. This conclusion was supported by conformational analysis executed semi-empirically with computational methods (DFT method) and NMR spectroscopy. **A6D** dye showed a strong donor–acceptor behaviour by virtue of its asymmetrical distribution of functional blocks, ensuring high charge separation in the excited state as well as an extended spectrum of absorption (reaching NIR region). Once implemented in *p*-DSCs, the corresponding device reaches a photo-conversion efficiency of 0.15 % preserving also a fair AVT as high as 8 %. This is mainly due to a reduction of the unwanted recombination reaction rate as proved by light-modulated JV investigation. The convergent block-synthesis of **A6D** allows the operator to combine the single blocks separately synthesized with alternative configurations. This is the case of the preparation of **D6D** with the tri-block configuration donor-π spacer- donor. At the basis of **D6D** synthesis there

was the aim of having a narrow absorption window which is shifted towards the blue part of the visible spectra. Favourable consequences are the high AVT values (38 %) and wave-selective behaviour. These are counterbalanced by the offset of displaying a very low photoconversion efficiency (0.007 %). The poor photoconversion results in **D6D** based devices are ascribable to the localization of both HOMO and LUMO in the oligothiophene spacer with little displacement of the excited electronic cloud from the site of excitation and consequent poor electron transfer properties in the photoactivated reduction process. Some experimental findings were successfully interpreted with DFT calculations. This will pave the way for an effective use of theoretical methods in the design of this type of functional materials. Newly designed and synthesized **A6D** dye produces photoconversion devices that reach comparatively very large efficiency values. However, compared to the state-of-art efficiency (2.51 % using NiO$_x$ as photoanode, PMI-6 T-TPA as sensitizer and Fe(acac) as redox mediator) our device produce quite lower power conversion efficiency. This is mainly ascribable to the presence of a Fe-based electrolyte. As such, in a forthcoming paper, we are planning to implement a new Fe-based redox mediator in combination with **A6D**, to approach SoA efficiency. Besides this, further amelioration could be reached through the optimization of the photocathode (both increasing its thickness and implementing a blocking layer) and the use of additives for molecular disaggregation of dyes in the anchored state. In conclusion, the convergent block-synthesis shows great potential for the design of sensitizers having specific properties.

Declaration of Competing Interest

The authors declare that they have no known competing financial interests or personal relationships that could have appeared to influence the work reported in this paper.

Appendix A. Supplementary data

Supplementary data to this article can be found online at https://doi.org/10.1016/j.solener.2023.112143.

References

[1] P. Nejat, F. Jomehzadeh, M.M. Taheri, M. Gohari, M.Z. Abd, Majid, A global review of energy consumption, CO2 emissions and policy in the residential sector (with an overview of the top ten CO2 emitting countries), Renew. Sustain. Energy Rev. 43 (2015) 843–862, https://doi.org/10.1016/j.rser.2014.11.066.

[2] N.S. Lewis, D.G. Nocera, Powering the planet: Chemical challenges in solar energy utilization, Proceedings of the National Academy of Sciences. 103 (2006) 15729–15735. https://doi.org/10.1073/pnas.0603395103.

[3] S.E. Hosseini, M.A. Wahid, Hydrogen production from renewable and sustainable energy resources: Promising green energy carrier for clean development, Renew. Sustain. Energy Rev. 57 (2016) 850–866, https://doi.org/10.1016/j.rser.2015.12.112.

[4] B. O'Regan, M. Grätzel, A low-cost, high-efficiency solar cell based on dye-sensitized colloidal TiO$_2$ films, Nature 353 (1991) 737–740, https://doi.org/10.1038/353737a0.

[5] M. Freitag, J. Teuscher, Y. Saygili, X. Zhang, F. Giordano, P. Liska, J. Hua, S. M. Zakeeruddin, J.-E. Moser, M. Grätzel, A. Hagfeldt, Dye-sensitized solar cells for efficient power generation under ambient lighting, Nat Photon. 11 (2017) 372–378, https://doi.org/10.1038/nphoton.2017.60.

[6] A.B. Muñoz-García, I. Benesperi, G. Boschloo, J.J. Concepcion, J.H. Delcamp, E. A. Gibson, G.J. Meyer, M. Pavone, H. Pettersson, A. Hagfeldt, M. Freitag, Dye-sensitized solar cells strike back, Chem. Soc. Rev. 50 (2021) 12450–12550, https://doi.org/10.1039/d0cs01336f.

[7] Y. Ren, D. Zhang, J. Suo, Y. Cao, F.T. Eickemeyer, N. Vlachopoulos, S. M. Zakeeruddin, A. Hagfeldt, M. Grätzel, Hydroxamic acid pre-adsorption raises the efficiency of cosensitized solar cells, Nature 613 (2023) 60–65, https://doi.org/10.1038/s41586-022-05460-z.

[8] J. He, H. Lindström, A. Hagfeldt, S.-E. Lindquist, Dye-Sensitized Nanostructured p-Type Nickel Oxide Film as a Photocathode for a Solar Cell, J. Phys. Chem. B 103 (1999) 8940–8943, https://doi.org/10.1021/jp991681r.

[9] F. Odobel, L. Le Pleux, Y. Pellegrin, E. Blart, New photovoltaic devices based on the sensitization of p-type semiconductors: Challenges and opportunities, Acc. Chem. Res. 43 (2010) 1063–1071, https://doi.org/10.1021/ar900275b.

[10] A. Nattestad, M. Ferguson, R. Kerr, Y.-B. Cheng, U. Bach, Dye-sensitized nickel(II) oxide photocathodes for tandem solar cell applications, Nanotechnology 19 (2008), 295304, https://doi.org/10.1088/0957-4484/19/29/295304.

[11] C. Cavallo, F. Di Pascasio, A. Latini, M. Bonomo, D. Dini, Nanostructured Semiconductor Materials for Dye-Sensitized Solar Cells, J. Nanomater. 2017 (2017) 5323164, https://doi.org/10.1155/2017/5323164.

[12] Y. Farré, M. Raissi, A. Fihey, Y. Pellegrin, E. Blart, D. Jacquemin, F. Odobel, A blue diketopyrrolopyrrole sensitizer with high efficiency in nickel-oxide-based dye-sensitized solar cells, ChemSusChem 10 (2017) 2618–2625, https://doi.org/10.1002/cssc.201700468.

[13] F. Odobel, Y. Pellegrin, E.A. Gibson, A. Hagfeldt, A.L. Smeigh, L. Hammarström, Recent advances and future directions to optimize the performances of p-type dye-sensitized solar cells, Coord. Chem. Rev. 256 (2012) 2414–2423, https://doi.org/10.1016/j.ccr.2012.04.017.

[14] E. Benazzi, J. Mallows, G.H. Summers, F.A. Black, E.A. Gibson, Developing photocathode materials for p-type dye-sensitized solar cells, J. Mater. Chem. C Mater. 7 (2019) 10409–10445, https://doi.org/10.1039/c9tc01822k.

[15] S. Sheehan, G. Naponiello, F. Odobel, D.P. Dowling, A. Di Carlo, D. Dini, Comparison of the photoelectrochemical properties of RDS NiO thin films for p-type DSCs with different organic and organometallic dye-sensitizers and evidence of a direct correlation between cell efficiency and charge recombination, J. Solid State Electrochem. 19 (2015) 975–986, https://doi.org/10.1007/s10008-014-2703-9.

[16] M. Urbani, M. Grätzel, M.K. Nazeeruddin, T. Torres, Meso-substituted porphyrins for dye-sensitized solar cells, Chem. Rev. 114 (2014) 12330–12396, https://doi.org/10.1021/cr5001964.

[17] M. Borgström, E. Blart, G. Boschloo, E. Mukhtar, A. Hagfeldt, L. Hammarström, F. Odobel, Sensitized hole injection of phosphorus porphyrin into NiO: Toward new photovoltaic devices, J. Phys. Chem. B 109 (2005) 22928–22934, https://doi.org/10.1021/jp054034a.

[18] A. Maufroy, L. Favereau, F.B. Anne, Y. Pellegrin, E. Blart, M. Hissler, D. Jacquemin, F. Odobel, Synthesis and properties of push–pull porphyrins as sensitizers for NiO based dye-sensitized solar cells, J Mater Chem A Mater. 3 (2015) 3908–3917, https://doi.org/10.1039/C4TA05974C.

[19] J. Lu, Z. Liu, N. Pai, L. Jiang, U. Bach, A.N. Simonov, Y. Cheng, L. Spiccia, Molecular Engineering of Zinc-Porphyrin Sensitisers for p-Type Dye-Sensitised Solar Cells, ChemPlusChem 83 (2018) 711–720, https://doi.org/10.1002/cplu.201800104.

[20] A. Carella, F. Borbone, R. Centore, Research progress on photosensitizers for DSSC, Front. Chem. 6 (2018) 481, https://doi.org/10.3389/fchem.2018.00481.

[21] Y. Ni, J. Wu, Far-red and near infrared BODIPY dyes: synthesis and applications for fluorescent pH probes and bio-imaging, Org. Biomol. Chem. 12 (2014) 3774, https://doi.org/10.1039/c3ob42554a.

[22] K. Umezawa, D. Citterio, K. Suzuki, New Trends in Near-Infrared Fluorophores for Bioimaging, Anal. Sci. 30 (2014) 327–349, https://doi.org/10.2116/analsci.30.327.

[23] M.-E. Ragoussi, T. Torres, Modern Synthetic Tools Toward the Preparation of Sophisticated Phthalocyanine-Based Photoactive Systems, Chem. Asian J. 9 (2014) 2676–2707, https://doi.org/10.1002/asia.201402311.

[24] G.H. Summers, J.-F. Lefebvre, F.A. Black, E. Stephen Davies, E.A. Gibson, T. Pullerits, C.J. Wood, K. Zidek, Design and characterisation of bodipy sensitizers for dye-sensitized NiO solar cells, PCCP 18 (2016) 1059–1070, https://doi.org/10.1039/C5CP05177K.

[25] O. Langmar, C.R. Ganivet, A. Lennert, R.D. Costa, G. de la Torre, T. Torres, D. M. Guldi, Combining electron-accepting phthalocyanines and nanorod-like CuO electrodes for p-type dye-sensitized solar cells, Angew. Chem. Int. Ed. 54 (2015) 7688–7692, https://doi.org/10.1002/anie.201501550.

[26] D. Dini, M.J.F. Calvete, M. Hanack, M. Meneghetti, Indium phthalocyanines with different axial ligands: a study of the influence of the structure on the photophysics and optical limiting properties, Chem. A Eur. J. 112 (2008) 8515–8522, https://doi.org/10.1021/jp802960s.

[27] L. Favereau, J. Warnan, Y. Pellegrin, E. Blart, M. Boujtita, D. Jacquemin, F. Odobel, Diketopyrrolopyrrole derivatives for efficient NiO-based dye-sensitized solar cells, Chem. Commun. 49 (2013) 8018, https://doi.org/10.1039/c3cc44232b.

[28] L. Zhang, L. Favereau, Y. Farré, E. Mijangos, Y. Pellegrin, E. Blart, F. Odobel, L. Hammarström, Ultrafast and slow charge recombination dynamics of diketopyrrolopyrrole–NiO dye sensitized solar cells, PCCP 18 (2016) 18515–18527, https://doi.org/10.1039/C6CP01762B.

[29] Y. Farré, L. Zhang, Y. Pellegrin, A. Planchat, E. Blart, M. Boujtita, L. Hammarström, D. Jacquemin, F. Odobel, Second Generation of Diketopyrrolopyrrole Dyes for NiO-Based Dye-Sensitized Solar Cells, J. Phys. Chem. C 120 (2016) 7923–7940, https://doi.org/10.1021/acs.jpcc.5b12489.

[30] C.-H. Chang, Y.-C. Chen, C.-Y. Hsu, H.-H. Chou, J.T. Lin, Squaraine-Arylamine Sensitizers for Highly Efficient p-Type Dye-Sensitized Solar Cells, Org. Lett. 14 (2012) 4726–4729, https://doi.org/10.1021/ol301860w.

[31] J. Warnan, J. Gardner, L. Le Pleux, J. Petersson, Y. Pellegrin, E. Blart, L. Hammarström, F. Odobel, Multichromophoric Sensitizers Based on Squaraine for NiO Based Dye-Sensitized Solar Cells, J. Phys. Chem. C 118 (2014) 103–113, https://doi.org/10.1021/jp408900x.

[32] M. Bonomo, D. Saccone, C. Magistris, A. DiCarlo, C. Barolo, D. Dini, D. Dini, Effect of alkyl chain length on the sensitizing action of substituted non symmetric squaraines for p-type dye-sensitized solar cells, ChemElectroChem 4 (2017) 2385–2397, https://doi.org/10.1002/celc.201700191.

[33] G. Naponiello, I. Venditti, V. Zardetto, D. Saccone, A. Di Carlo, I. Fratoddi, C. Barolo, D. Dini, Photoelectrochemical characterization of squaraine-sensitized nickel oxide cathodes deposited via screen-printing for p-type dye-sensitized solar cells, Appl. Surf. Sci. 356 (2015) 911–920, https://doi.org/10.1016/j.apsusc.2015.08.171.

[34] M. Bonomo, N. Barbero, F. Matteocci, A. Di Carlo, C. Barolo, D. Dini, Beneficial effect of electron-withdrawing groups on the sensitizing action of squaraines for p-type dye-sensitized solar cells, J. Phys. Chem. C 120 (2016) 16340–16353, https://doi.org/10.1021/acs.jpcc.6b03965.

[35] M. Bonomo, A. Carella, R. Centore, A. Di Carlo, D. Dini, A. Di Carlo, D. Dini, First examples of pyran based colorants as sensitizing agents of p-type dye-sensitized solar cells, J. Electrochem. Soc. 164 (2017) F1412–F1418, https://doi.org/10.1149/2.0671713jes.

[36] M. Bonomo, A. Di Carlo, R. Centore, D. Dini, A. Carella, New pyran-based dyes as efficient sensitizers of p-type dye-sensitized solar cells, Sol. Energy 169 (2018) 237–241, https://doi.org/10.1016/j.solener.2018.04.050.

[37] L. Le Pleux, A.L. Smeigh, E. Gibson, Y. Pellegrin, E. Blart, G. Boschloo, A. Hagfeldt, L. Hammarström, F. Odobel, Synthesis, photophysical and photovoltaic investigations of acceptor-functionalized perylene monoimide dyes for nickel oxide p-type dye-sensitized solar cells, Energy Environ. Sci. 4 (2011) 2075–2084, https://doi.org/10.1039/c1ee01148k.

[38] T.T.T. Pham, S.K. Saha, D. Provost, Y. Farré, M. Raissi, Y. Pellegrin, E. Blart, S. Vedraine, B. Ratier, D. Aldakov, F. Odobel, J. Bouclé, Toward Efficient Solid-State p-Type Dye-Sensitized Solar Cells: The Dye Matters, J. Phys. Chem. C 121 (2017) 129–139, https://doi.org/10.1021/acs.jpcc.6b10513.

[39] A. Daoud, A. Cheknane, A. Meftah, J. Michel Nunzi, M. Shalabi, H.S. Hilal, Spatial separation strategies to control charge recombination and dye regeneration in p-type dye sensitized solar cells, Sol. Energy 236 (2022) 107–152, https://doi.org/10.1016/j.solener.2022.02.050.

[40] P. Qin, H. Zhu, T. Edvinsson, G. Boschloo, A. Hagfeldt, L. Sun, Design of an organic chromophore for P-type dye-sensitized solar cells, J. Am. Chem. Soc. 130 (2008) 8570–8571, https://doi.org/10.1021/ja8001474.

[41] M. Bonomo, D. Di Girolamo, M. Piccinni, D.P. Dowling, D. Dini, Electrochemically deposited NiO films as a blocking layer in p-type dye-sensitized solar cells with an impressive 45% fill factor, Nanomaterials 10 (2020), https://doi.org/10.3390/nano10010167.

[42] C.J. Wood, G.H. Summers, E.A. Gibson, Increased photocurrent in a tandem dye-sensitized solar cell by modifications in push–pull dye-design, Chem. Commun. 51 (2015) 3915–3918, https://doi.org/10.1039/C4CC10230D.

[43] F. Wu, S. Zhao, C. Zhong, Q. Song, L. Zhu, Insights into dye design for efficient p-type photoelectrodes: effect of oligothiophene length between the donor and the NiO surface, RSC Adv. 5 (2015) 93652–93658, https://doi.org/10.1039/C5RA19854B.

[44] F. Wu, L. Zhu, S. Zhao, Q. Song, C. Yang, Engineering of organic dyes for highly efficient p-type dye-sensitized solar cells, Dyes Pigm. 124 (2016) 93–100, https://doi.org/10.1016/j.dyepig.2015.09.008.

[45] I.R. Perera, T. Daeneke, S. Makuta, Z. Yu, Y. Tachibana, A. Mishra, P. Bäuerle, C. A. Ohlin, U. Bach, L. Spiccia, Application of the tris(acetylacetonato)iron(III)/(II) redox couple in p-type dye-sensitized solar cells, Angewandte Chemie - International Edition. 54 (2015) 3758–3762, https://doi.org/10.1002/anie.201409877.

[46] M. Bonomo, E.J. Ekoi, A.G. Marrani, A.Y. Segura Zarate, D.P. Dowling, C. Barolo, D. Dini, NiO/ZrO$_2$ nanocomposites as photocathodes of tandem DSCs with higher photoconversion efficiency with respect to parent single-photoelectrode p-DSCs,

Sustain, Energy Fuels 5 (2021) 4736–4748, https://doi.org/10.1039/D1SE00566A.

[47] K.A. Click, D.R. Beauchamp, B.R. Garrett, Z. Huang, C.M. Hadad, Y. Wu, A double-acceptor as a superior organic dye design for p-type DSSCs: high photocurrents and the observed light soaking effect, Phys. Chem. Chem. Phys. Phys. Chem. Chem. Phys. 16 (2014) 26103–26111, https://doi.org/10.1039/c4cp04010d.

[48] Z. Liu, W. Li, S. Topa, X. Xu, X. Zeng, Z. Zhao, M. Wang, W. Chen, F. Wang, Y. B. Cheng, H. He, Fine tuning of fluorene-based dye structures for high-efficiency p-type dye-sensitized solar cells, ACS Appl. Mater. Interfaces 6 (2014) 10614–10622, https://doi.org/10.1021/am5022396.

[49] A.I. Vogel, A.R. Tatchell, B.S. Furniss, A.J. Hannaford, P.W.G. Smith, Textbook of Practical Organic Chemistry, 5th ed., Prentice-Hall, 1996.

[50] G.R. Van Hecke, W. DeW, Horrocks, dietertiary phosphine complexes of nickel. spectral, magnetic, and proton resonance studies. a planar-tetrahedral equilibrium, Inorg. Chem. 5 (1966) 1968–1974, https://doi.org/10.1021/ic50045a029.

[51] H.J. Dauben, L.L. McCoy, N-Bromosuccinimide. I. Allylic Bromination, a General Survey of Reaction Variables 1–3, J. Am. Chem. Soc. 81 (1959) 4863–4873, https://doi.org/10.1021/ja01527a027.

[52] V. D'Annibale, C.G. Chen, M. Bonomo, D. Dini, M. D'Abramo, P1 push-pull dye as a case study in QM/MM theoretical characterization for dye-sensitized solar cell organic chromophores**, ChemistrySelect 8 (2023), https://doi.org/10.1002/slct.202204904.

[53] T. Yanai, D.P. Tew, N.C. Handy, A new hybrid exchange–correlation functional using the Coulomb-attenuating method (CAM-B3LYP), Chem. Phys. Lett. 393 (2004) 51–57, https://doi.org/10.1016/j.cplett.2004.06.011.

[54] M. Ernzerhof, G.E. Scuseria, Assessment of the Perdew–Burke–Ernzerhof exchange-correlation functional, J. Chem. Phys. 110 (1999) 5029–5036, https://doi.org/10.1063/1.478401.

[55] C. Adamo, V. Barone, Toward reliable density functional methods without adjustable parameters: The PBE0 model, J. Chem. Phys. 110 (1999) 6158–6170, https://doi.org/10.1063/1.478522.

[56] Y. Zhao, D.G. Truhlar, The M06 suite of density functionals for main group thermochemistry, thermochemical kinetics, noncovalent interactions, excited states, and transition elements: Two new functionals and systematic testing of four M06-class functionals and 12 other function, Theor. Chem. Acc. 120 (2008) 215–241, https://doi.org/10.1007/s00214-007-0310-x.

[57] R. Mengji, C. Acharya, V. Vangala, A. Jana, A lysosome-specific near-infrared fluorescent probe for *in vitro* cancer cell detection and non-invasive *in vivo* imaging, Chem. Commun. 55 (2019) 14182–14185, https://doi.org/10.1039/C9CC07322A.

[58] T. Ishiyama, M. Murata, N. Miyaura, Palladium(0)-Catalyzed Cross-Coupling Reaction of Alkoxydiboron with Haloarenes: A Direct Procedure for Arylboronic Esters, J. Org. Chem. 60 (1995) 7508–7510, https://doi.org/10.1021/jo00128a024.

[59] K. Tamao, K. Sumitani, M. Kumada, Selective carbon-carbon bond formation by cross-coupling of Grignard reagents with organic halides, Catalysis by Nickel-Phosphine Complexes, J Am Chem Soc. 94 (1972) 4374–4376, https://doi.org/10.1021/ja00767a075.

[60] J.F. Hartwig, Carbon−Heteroatom Bond-Forming Reductive Eliminations of Amines, Ethers, and Sulfides, Acc. Chem. Res. 31 (1998) 852–860, https://doi.org/10.1021/ar970282g.

[61] R.A. Widenhoefer, S.L. Buchwald, Electronic dependence of C−O reductive elimination from palladium (Aryl)neopentoxide complexes, J. Am. Chem. Soc. 120 (1998) 6504–6511, https://doi.org/10.1021/ja9806581.

[62] M.R. Netherton, G.C. Fu, Air-stable trialkylphosphonium salts: simple, practical, and versatile replacements for air-sensitive trialkylphosphines, Appl. Stoichiometric Catal. Process. Org Lett. 3 (2001) 4295–4298, https://doi.org/10.1021/ol016971g.

[63] A.F. Littke, C. Dai, G.C. Fu, Versatile catalysts for the suzuki cross-coupling of arylboronic acids with aryl and vinyl halides and triflates under mild conditions, J. Am. Chem. Soc. 122 (2000) 4020–4028, https://doi.org/10.1021/ja0002058.

[64] B. Liu, Q. Liu, D. You, X. Li, Y. Naruta, W. Zhu, Molecular engineering of indoline based organic sensitizers for highly efficient dye-sensitized solar cells, J. Mater. Chem. 22 (2012) 13348–13356, https://doi.org/10.1039/c2jm31704d.

[65] T.-J. Lin, S.-T. Lin, Theoretical study on the torsional potential of alkyl, donor, and acceptor substituted bithiophene: the hidden role of noncovalent interaction and backbone conjugation, PCCP 17 (2015) 4127–4136, https://doi.org/10.1039/C4CP05379F.

[66] M. Weidelener, A. Mishra, A. Nattestad, S. Powar, A.J. Mozer, E. Mena-Osteritz, Y.-B. Cheng, U. Bach, P. Bäuerle, Synthesis and characterization of perylene–bithiophene–triphenylamine triads: studies on the effect of alkyl-substitution in p-type NiO based photocathodes, J. Mater. Chem. 22 (2012) 7366, https://doi.org/10.1039/c2jm16847b.

[67] J. Cremer, Novel head-to-tail coupled oligo(3-hexylthiophene) derivatives for photovoltaic applications, Universität Ulm, 2005.

[68] S. Klod, E. Kleinpeter, Ab initio calculation of the anisotropy effect of multiple bonds and the ring current effect of arenes—application in conformational and configurational analysis, Journal of the Chemical Society, Perkin, Transactions 2 (2001) 1893–1898, https://doi.org/10.1039/b009809o.

[69] M. Feroci, T. Civitarese, F. Pandolfi, R. Petrucci, D. Rocco, D. Zane, G. Zollo, L. Mattiello, Electrochemical studies of new donor-acceptor oligothiophenes, ChemElectroChem 6 (2019) 4016–4021, https://doi.org/10.1002/celc.201900920.

[70] F. Pandolfi, M. Bortolami, M. Feroci, L. Mattiello, V. Scarano, D. Rocco, Electrochemistry: a useful tool in the synthesis of oligothiophenes, Curr. Org. Chem. 25 (2021) 2028–2036, https://doi.org/10.2174/1385272825666210715104931.

[71] N.T.Z. Potts, T. Sloboda, M. Wächtler, R.A. Wahyuono, V. D'Annibale, B. Dietzek, U.B. Cappel, E.A. Gibson, Probing the dye-semiconductor interface in dye-sensitized NiO solar cells, J. Chem. Phys. 153 (2020), 184704, https://doi.org/10.1063/5.0023000.

[72] O. Langmar, D. Saccone, A. Amat, S. Fantacci, G. Viscardi, C. Barolo, R.D. Costa, D. M. Guldi, P-type Squaraines Designing to Control Charge Injection and Recombination Processes in NiO based p-type Dye-Sensitized Solar Cells, ChemSusChem (2017), https://doi.org/10.1002/cssc.201700152.

[73] M. Bonomo, A. Carella, F. Borbone, L. Rosato, D. Dini, L. Gontrani, New pyran-based molecules as both n- and p-type sensitizers in semi-transparent Dye Sensitized Solar Cells, Dyes Pigm. 175 (2020), 108140, https://doi.org/10.1016/j.dyepig.2019.108140.

[74] E.J. Baerends, O.V. Gritsenko, R. van Meer, The Kohn-Sham gap, the fundamental gap and the optical gap: the physical meaning of occupied and virtual Kohn-Sham orbital energies, PCCP 15 (2013) 16408, https://doi.org/10.1039/c3cp52547c.

[75] J. Zirzlmeier, S. Schrettl, J.C. Brauer, E. Contal, L. Vannay, É. Brémond, E. Jahnke, D.M. Guldi, C. Corminboeuf, R.R. Tykwinski, H. Frauenrath, Optical gap and fundamental gap of oligoynes and carbyne, Nat. Commun. 11 (2020) 4797, https://doi.org/10.1038/s41467-020-18496-4.

[76] J.-L. Bredas, Mind the gap!, Mater. Horiz. 1 (2014) 17–19, https://doi.org/10.1039/C3MH00098B.

[77] C.M. Cardona, W. Li, A.E. Kaifer, D. Stockdale, G.C. Bazan, Electrochemical Considerations for Determining Absolute Frontier Orbital Energy Levels of Conjugated Polymers for Solar Cell Applications, Adv. Mater. 23 (2011) 2367–2371, https://doi.org/10.1002/adma.201004554.

[78] J.C.S. Costa, R.J.S. Taveira, C.F.R.A.C. Lima, A. Mendes, L.M.N.B.F. Santos, Optical band gaps of organic semiconductor materials, Opt Mater (amst) 58 (2016) 51–60, https://doi.org/10.1016/j.optmat.2016.03.041.

[79] M. Bonomo, A. Di Carlo, D. Dini, Study of the influence of the i-based electrolyte composition on the photoconversion properties of p-type dye-sensitized solar cells, J. Electrochem. Soc. 165 (2018) H889–H896, https://doi.org/10.1149/2.0261814jes.